

SPECTROSCOPIC DIAGNOSTICS OF AN ARC JET HEATED AIR PLASMA

by

Larry Howard Mack, Jr., B.S.

11-75  
(S. H. Mack)  
01-9-75

THESIS

Presented to the Faculty of  
The University of Houston - Clear Lake  
in Partial fulfillment  
of the Requirements  
for the Degree of

MASTER OF SCIENCE

THE UNIVERSITY OF HOUSTON CLEAR LAKE

December, 1996

Copyright 1996, Larry H. Mack, Jr.  
All Rights Reserved

## ACKNOWLEDGEMENTS

I would like to thank my professors, Mohammad Rob and William Lawrence for their efforts in helping me understand the physics of my research project as well as their guidance and patience. I would also like to thank my NASA advisors Drs. Sivaram Arepalli and Carl Scott, for if it were not for them this thesis could not have been accomplished. They offered great insight into the field along with guidance of the project. They also funded the project through grants from NASA to the University of Houston, which will hopefully continue and create a working relationship between industry and the university system. In addition to these advisors I would also thank the personnel of NASA's building 222. Without their late hours of arc jet runs this project also would not have been possible. One more key person who donated a considerable amount of time and knowledge to the analysis side of my project was Dr. Christophe Laux of the Stanford University. A special thanks to Dr. Laux for his time and effort.

Finally, I would like to thank my wife Vivian and my parents Larry Sr. and Charlene for all of their support, patience, and ability to leave me alone on those long, writing weekends!

## ABSTRACT

## SPECTROSCOPIC DIAGNOSTICS OF AN ARC JET HEATED AIR PLASMA

Larry Howard Mack, Jr, M.S.

The University of Houston Clear Lake, 1996

Thesis Chair: George Blanford

Spectral radiation measurements were made in the range of 200 to 900 nm across a section of the plenum of an arc jet wind tunnel using a series of optical fibers. The spectra contained line radiation from Oxygen and Nitrogen atoms and molecular radiation from  $N_2^+$ ,  $N_2$ , and NO. Abel inversion technique is used to obtain radial distribution of the spectra. The analysis yielded radial profiles of the electronic excitation, vibrational and rotational temperatures of the flow field. Spectral fitting yielded branching ratios for different vibrational and rotational bands. Relatively mild flow conditions, i.e. enthalpy and mass flow rate, were used for prolonged measurements of up to and over two hours to establish the best experimental methods of temperature determinations. Signal to noise was improved by at least an order of magnitude enabling the molecular vibrational band heads of  $N_2^+$  (first negative system),  $N_2$  (second positive system), and NO ( $\beta$ ,  $\gamma$ ,  $\delta$ , and  $\epsilon$  systems) to be resolved in the lower ultraviolet wavelength regions. The increased signal to noise ratio also enabled partial resolution of the rotational lines of  $N_2^+$  and  $N_2$  in certain regions of minimal overlap. Comparison of the spectra with theoretical models such as the NEQAIR2 code are presented and show potential for fitting the spectra when reliable calibration is performed for the complete wavelength range.

## TABLE OF CONTENTS

Abstract .....	iv
Table of Contents .....	v
List of Tables .....	vii
List of Figures .....	viii
Chapter 1. Overview of Arc-Heated Air Plasma Flows	
1.1 Introduction .....	1
1.2 Plasma flow diagnostics using optical techniques .....	3
1.3 Research objectives .....	5
Chapter 2. Facility and Instrumentation	
2.1 General description-arc jet wind tunnel .....	7
2.2 Plenum design .....	10
2.3 Optical fiber / lens adapter .....	14
2.4 Spectrometers .....	17
2.5 PMT / lockin / SRS data acquisition .....	18
2.6 Optical multichannel analyzer (OMA) .....	19
2.7 Experimental procedures .....	20
2.7.1 Optical alignment .....	20
2.7.2 Instrumentation and data acquisition .....	21
2.7.3 Calibration .....	23
2.7.3.a Wavelength .....	23
2.7.3.b Intensity .....	24

Chapter 3.	Theory and Background	
3.1	Plasma emission spectroscopy . . . . .	28
3.2	LTE temperature distribution in the plasma . . . . .	29
3.3	Molecular properties . . . . .	33
3.3.1	Vibrational temperature . . . . .	33
3.3.2	Rotational temperature . . . . .	34
3.4	Abel inversion method. . . . .	35
Chapter 4.	Results and Discussion	
4.1	Temperature determination of excited electronic states . . . . .	38
4.2	Spectral fitting using NEQAIR 2 . . . . .	43
4.3	Rotational temperature determination of the 0-1 band of $N_2^+$ (first negative) . . . . .	51
Chapter 5.	Conclusion	
5.1	Contributions of this thesis . . . . .	57
5.2	Recommendations for future work . . . . .	58
References	. . . . .	59

## LIST OF TABLES

### CHAPTER 1

1.1	Various Methods used for Determination of Flow Parameters . . . . .	4
-----	---	---

### CHAPTER 2

2.1	Typical operating conditions used for the lock-in amplifier . . . . .	22
-----	---	----

### CHAPTER 3

3.1	Atomic Transitions Considered for the LTE Temperature Measurement of Nitrogen . . . . .	31
3.2	Atomic Transitions Considered for the LTE Temperature Measurement of Oxygen . . . . .	32
3.3	Strong Vibrational Bands in the Air Plasma . . . . .	33

### CHAPTER 4

4.1	Measured (exp) and Theoretical (th) branching ratios (br) for the $N_2^+$ First Negative band system. . . . .	51
-----	---	----

## LIST OF FIGURES

### CHAPTER 1

- 1.1 Catalytic recombination of atoms and molecules on thermal protection materials during reentry into the earth's atmosphere. . . . . 2

### CHAPTER 2

- 2.1 Picture of the arc jet wind tunnel test facility. Arrows show where the optical fibers were inserted into the heater . . . . . 8
- 2.2 (a) Schematic for the arc jet wind tunnel used in previous 2-inch plenum region design. (b) The design of the arc jet used previously . . . . . 11
- 2.3 Picture of the copper ring used in the plenum of the arc jet wind tunnel. 12
- 2.4 (a) View of the anode, plenum and nozzle regions. (b) The design of the arc jet wind tunnel used in the present data collection . . . . . 13
- 2.5 Optical line-of-sight configuration for the plenum ring . . . . . 15
- 2.6 (a) Illustration and (b) fiber optic arrangement used for collection of the spectral radiation from the plenum of the arc jet . . . . . 16
- 2.7 Experimental configuration for the intensity calibration using a standard tungsten ribbon filament lamp . . . . . 26
- 2.8 Relative spectral response of the detection system over the wavelength range of interest . . . . . 27

### CHAPTER 3

- 3.1 The Abel diagram for emission conversion of line-of-sight to radial coordinates . . . . . 36

## CHAPTER 4

4.1	Experimental emission spectra of the plenum air plasma . . . . .	40
4.2	Abel inverted spectra of the plenum air plasma . . . . .	41
4.3	Boltzmann distribution and radial temperature profile for oxygen and nitrogen . . . . .	42
4.4	Experimental emission spectra showing vibrational bands of $N_2^+$ (first negative), $N_2$ (second positive), NO . . . . .	44
4.5	Abel inversion spectra of the vibrational bands of $N_2^+$ (1st negative), $N_2$ (second positive), and NO . . . . .	46
4.6	Radial temperature profile of $N_2^+$ first negative band heads . . . . .	47
4.7	Comparison of experimental and computed (NEQAIR2) molecular nitrogen spectra of the plenum air plasma. The experimental spectra is Abel inverted and is for $y=2.5\text{cm}$ . . . . .	49
4.8	Ratio of the intensity of various band heads plotted against the product of $A$ and $\Delta E$ to show the estimated calibration error across the spectrum .	50
4.9	Experimental and computed (NEQAIR2) nitrogen spectra of the plenum air plasma . . . . .	52
4.10	Experimental and computed nitrogen rotational line spectra from the 0-1 band of the plenum air plasma. 1 and 1.5 inch off-axis positions . . . . .	54
4.11	Experimental and computed nitrogen rotational line spectra from the 0-1 band of the plenum air plasma. 2 and 2.5 inch off-axis positions . . . . .	55
4.12	Radial temperature profile of the nitrogen rotational spectra . . . . .	56



## CHAPTER 1

### Overview of Arc-Heated Air Plasma Flows

#### 1.1 Introduction

Thermal protection systems for spacecraft reentering the earth's atmosphere have been critical since the earliest designs of reentry vehicles. The high heating environment of the reentry has long been a concern and continues to be critical in orbiters' need for thermal protection materials (TPS) which will be lighter and less costly. These lighter materials will enable larger payloads to be carried as well as keeping the cost per mission to a minimum. Testing these materials requires a facility that could: simulate the harsh temperatures of reentry; enable the designers to retest many materials in various conditions; and accomplish all of this with a minimum cost and a maximum of safety. The present arc-jet wind tunnel facility was built in 1966 for testing of these thermal protection materials.

Arc-heated wind tunnels produce high enthalpy, high velocity flows inside an evacuated chamber. Material samples, as well as models designed to simulate spacecraft structures, are immersed in this flow to test their ability to withstand the most extreme of conditions. The success of these materials for suitable thermal protection depends on how well the environment is simulated at the testing point by comparing the expected conditions with measured conditions. Determining this environment requires complex theoretical and experimental procedures which will be discussed to some extent in the following chapters.

Arc-jet facilities are also used in estimating catalytic recombination rates of atoms on test surfaces. See figure 1.1. The molecules are dissociated into atoms in the high thermal

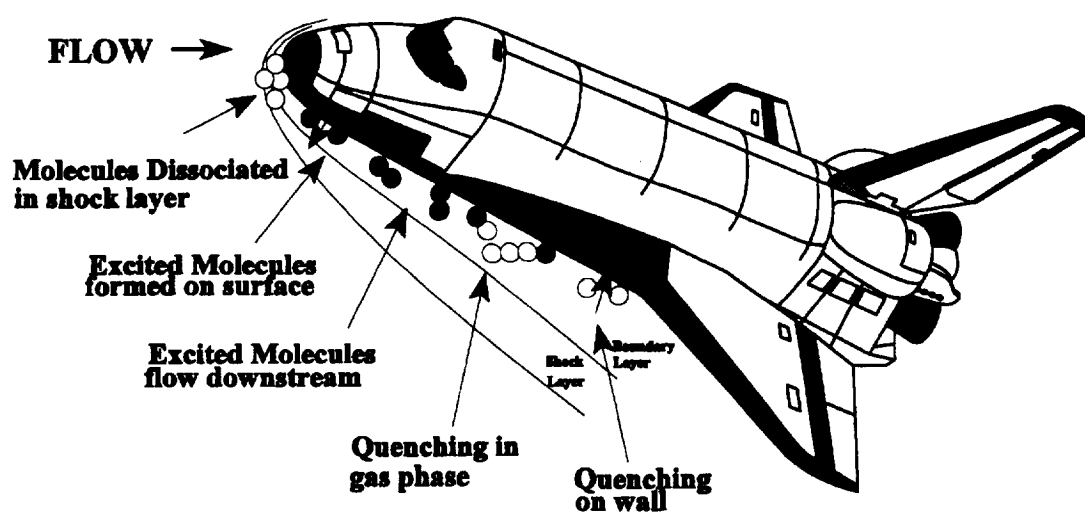


**Figure 1.1-** Catalytic recombination of molecules dissociated upon reentry into the Earth's atmosphere by reusable space structures.

conditions of the flow and may recombine upon the surface of the test material. When the atoms recombine they transfer their heat of dissociation to the surface.<sup>1</sup> Therefore, the rate at which the atoms recombine affects the heat flux to the surface of the material. The heat flux is therefore dependent on the properties of the material as well as the properties of the flow that encounters the surfaces of these materials. The objective of this project is to understand the properties of the flow.

## 1.2 Plasma flow diagnostics using optical techniques

An understanding of the flow properties of the arcjet involves many intrusive as well as non-intrusive methods of measurement that are identified in Table 1. Non-intrusive optical techniques include emission spectroscopy, absorption spectroscopy, laser-induced fluorescence and electron beam fluorescence. This particular project is associated with emission spectroscopy using line and continuum intensities.

The properties of the flow include the velocity, temperature, pressure, enthalpy, electron densities, and species concentrations. Because the free flow is in thermal and chemical nonequilibrium, measurements of the different modes of energy are needed. Thus, when characterizing this portion of the flow it is necessary to determine the vibrational, rotational, translational, excitation, and electronic temperatures of the various molecules. Studies of these free flow properties may be aided by gaining a better understanding of the flow properties in the settling chamber where the molecules may have enough time to thoroughly mix and relax to a state of thermo-chemical equilibrium. Since emission spectroscopy is the main method of measurement in this project, the various energy modes

can be measured to verify the equilibrium assumption. Arc-jets are typically run with atmospheric-like constituents, therefore the major species expected are  $N_2$ ,  $O_2$ ,  $N$ ,  $O$ ,  $NO$ ,  $N_2^+$ ,  $O_2^+$ ,  $N^+$ ,  $O^+$ ,  $NO^+$ , and electrons.<sup>2</sup>

**Table 1.1-** Various Methods used for Determination of Flow Parameters

PARAMETER TO BE MEASURED	METHOD OF MEASUREMENT
Velocity	- Laser-induced fluorescence, Doppler
Excitation temperature of atoms	- Emission spectroscopy line intensities
Vibrational and Rotational Temperatures of molecules	- Emission spectroscopy line intensities - Laser induced fluorescence - Electron beam fluorescence
Static electron temperature	- Emission spectroscopy line intensities - Continuum spectroscopy - Laser doppler profiles
Electron Density	- Emission spectroscopy continuum intensity line broadening, Doppler and Stark
Species concentrations	- Emission spectroscopy line intensities - Mass spectrometer

The dissociation of  $N_2$  and  $O_2$  molecules occurs when the enthalpy of the flow increases to substantial value. Molecular oxygen dissociates at a lower enthalpy than does molecular nitrogen. As the enthalpy is increased the relative concentrations of the individual species change according to the amount of dissociation required.<sup>3</sup> More discussion of the

dissociation will be discussed in the following chapters.

### 1.3 Research objectives

Many research programs have been under way for several years to characterize the free stream and shock layer of the arcjet, however, little work has been attempted in the settling region called the plenum. This plenum is considered to give information about the initial conditions of the free stream and obtaining the state of the plasma in this region will help in predicting the conditions of the flow as it impinges upon the test article. Park, et al,<sup>4</sup> gathered information for starting conditions by modelling the region between the electrodes in the arc region. We suspect that the presence of the arc complicates the development of a model of thermo-chemical equilibrium plasma used to get the initial conditions in the spectral fitting codes.

Therefore, this project involved collecting emissions from the plenum without interference from severe gradients in the region near the arc created by the electrodes of the heater. Since modelling the plenum region for temperature, electron densities, and species concentrations involves knowledge of the radial profile across the plasma, emissions were collected from multiple equidistant points across the flow with non-overlapping regions. A series of four optical fibers were designed to transfer the radiation to a spectrometer detection system. Once the data is collected, the Abel Inversion method is applied and temperatures can be calculated as a function of radial position. Three different temperatures will be the focus in this study and they include the electronic excitation, vibrational, and rotational states. It is assumed that the plasma is in thermodynamic equilibrium and,

therefore, all analysis will correspond accordingly. The methods for determining these temperatures will be discussed in Chapter 3.

## **CHAPTER 2**

### **The Experimental Facility**

#### **2.1 General description- arc jet wind tunnel**

The arc-heated wind tunnel is used to conduct thermal tests on thermal protection system (TPS) materials. Arc jets have proven to be the most useful devices for testing with because of its high heating rates and long test durations representative of local flight conditions. The facility at NASA/JSC, known as the 10 MW Atmospheric Reentry Materials and Structure Evaluation Facility (ARMSEF), has been in operation since 1968 to test, evaluate, and certify all materials used on manned United States spacecraft<sup>5</sup>.

The principal components of ARMSEF can be divided into three major regions; the evacuation system, the arc heater/conical nozzle system, and the control system. The arc heater's major components consist of the 10 MW arc heater, 10 MW DC solid state power supply, test gas supply system, and water cooling system. The evacuation system consists of two testing chambers, diffuser, boiler, and vacuum pumping system. The control system contains the control and computer rooms which remotely operate the system, collect the data, and control the video system which monitors the test chamber when it is in operation.

Although there are two test position chambers (TP1 and TP2) located at the facility, only TP2 was involved with this particular project. (See figure 2.1). TP2 is 3.6 meters in diameter and contains a 1.1 meter diameter, 6.1 meter long water-cooled diffuser. The chamber has 5 viewing windows for monitoring and inspection. The test chamber is evacuated by a four stage steam-ejector vacuum pumping system. Chamber pressures of 0.1

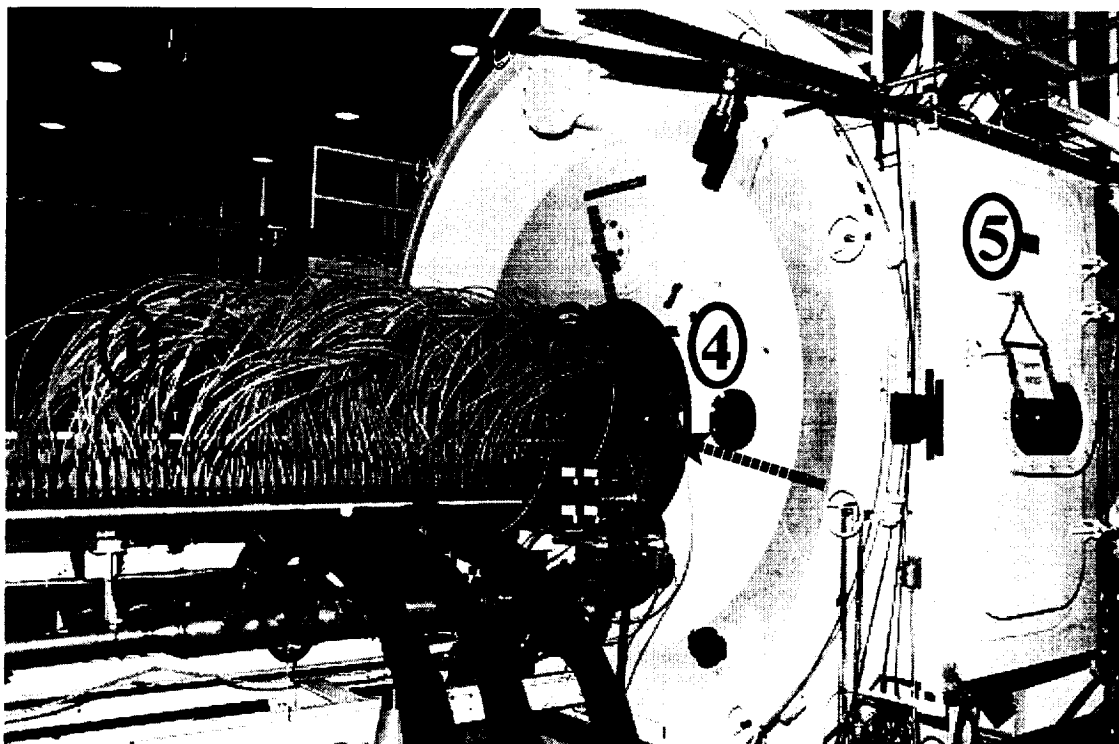


**Figure 2.1-** Picture of the arc jet wind tunnel test facility. Arrows show where the optical fibers were inserted into the heater. The numbers on the picture correspond to the following parts of the heater: 1) Cathode; 2) 600 psi water cooling lines; 3) anode; 4) conical nozzle; 5) ARMSEF TP2 chamber.



and 1 torr can be maintained by the system. The test chamber is cooled by a primary sealed closed loop coolant system with a capacity of 1340 gpm at 600 psi. A secondary cooling system with a capacity of 8000 gpm at 70 psi is used for heat extraction from the primary cooling system.

The arc heater consists of electrodes, heater column, plenum and conical nozzle region. The electrodes are powered by a solid state, d.c., silicon-controlled rectifier (SCR), water-cooled power supply rated for continuous operation at 10 MW. The heater consists of two electrodes with a conical copper anode and a tungsten button cathode as shown in Figure 2.2a. The heater column has a variable number of water-cooled, electrically insulated constrictor segments between the two electrodes. The test gas is injected between the electrodes with the  $N_2$  being injected closest to the cathode (as well as in various other positions) and the  $O_2$  injected downstream from the cathode to prevent oxidation of the tungsten. The test gas is stored in high pressure storage tanks and can be regulated for a variation of mass flow rates (13.6 to 158.9 g/sec) during testing.

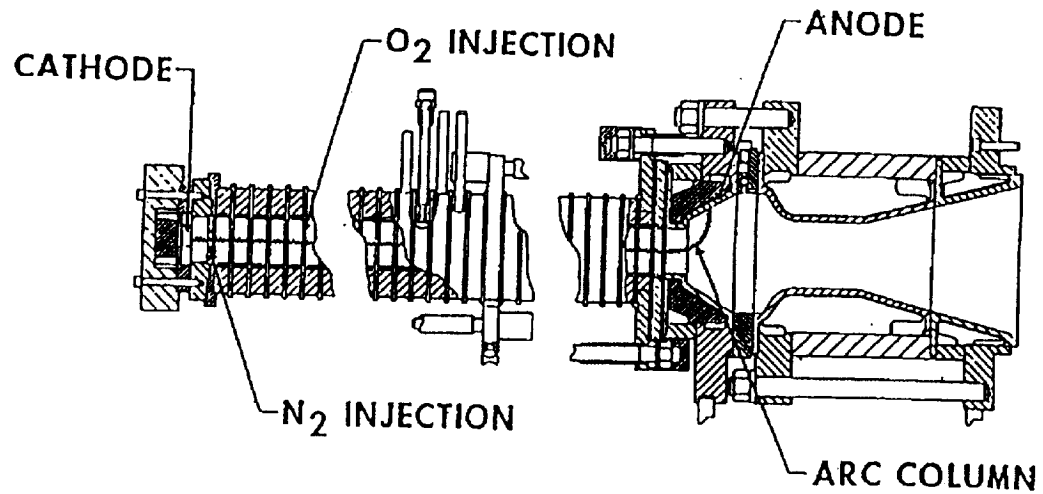
The plenum region consists of a water-cooled copper gas injection ring and a stack of water-cooled isolation disks. In its normal configuration the gas injection ring is connected to the anode and the stack is between the ring and the conical nozzle. However, in the present analysis the plenum was modified and this is explained in greater detail in the following section. The conical nozzle is the last part before the plasma reaches the free stream region. The nozzle is a converging then diverging nozzle with 15 degree half angle as in figure 2.2b. This configuration helps the plasma attain a state of thermo-chemical equilibrium before it expands to the free flow region.

The control or data acquisition system processes all measurements with a 256-channel computer-based data acquisition, processing and recording system. This system has the capability to abort interlock any of the 256 channels during a test when an abnormality occurs. During the testing up to ten channels of data can be plotted in real time. There are also features of video coverage for recording each run, pyrometer for surface temperature measurements, a pitot probe and heat flux gauges.<sup>6</sup>

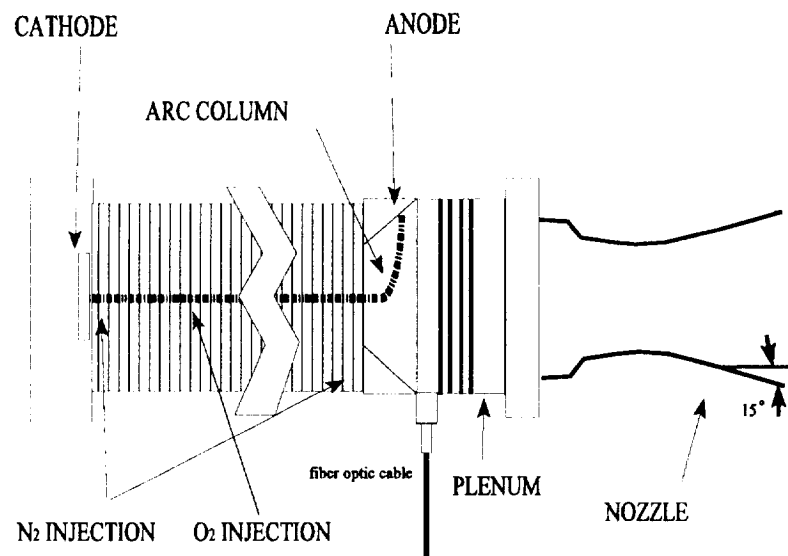
## 2.2 Plenum ring design

The plenum region was discussed in a general manner consistent with most of the testing done on the test position 2 (TP2). However, modification of the plenum was necessary for this experimental testing. In the previous work of Rob, et al<sup>7</sup>, a plenum ring was modified to collect light from the center most position of the flow by using a 200 micron core fiber as seen in figure 2.2. The spectra included some unidentified spectral features presumably due to the arc light rather than plenum radiation.

Also, to be able to determine the radial temperature and emission profiles, radiation would need to be collected from several positions across the flow. Therefore, the plenum ring was modified to allow light to be collected from four positions across the flow as well as placed away from the anode to minimize arc light as seen in figure 2.4. This allows the Abel Inversion method to be used with a fit of four equidistant points. Furthermore, the objective was to find the radial distribution in a thermo-chemical equilibrium plasma flow, without contributions from the arc light. The plenum ring was moved downstream of the electrode and connected directly to the conical nozzle with the isolation stack between the



(a)



(b)

**Figure 2.2-** (a) Schematic for the arcjet wind tunnel used in previous 2" plenum region design.  
 (b) The design of the arc jet wind tunnel used previously.

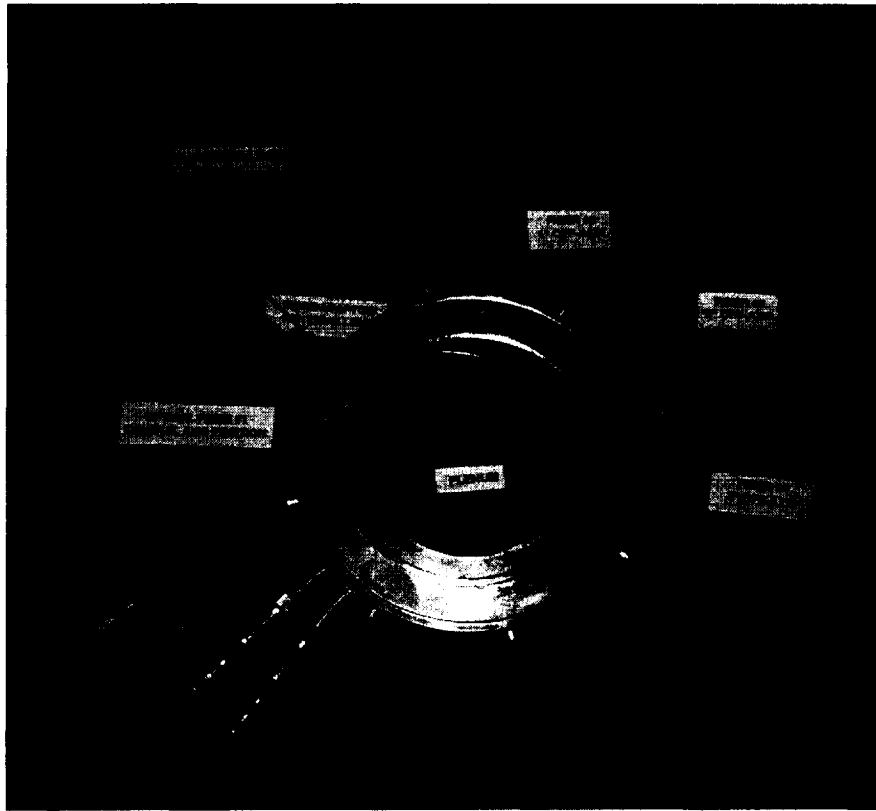


**Figure 2.3-** Picture of the copper ring used in the plenum of the arc jet wind tunnel.

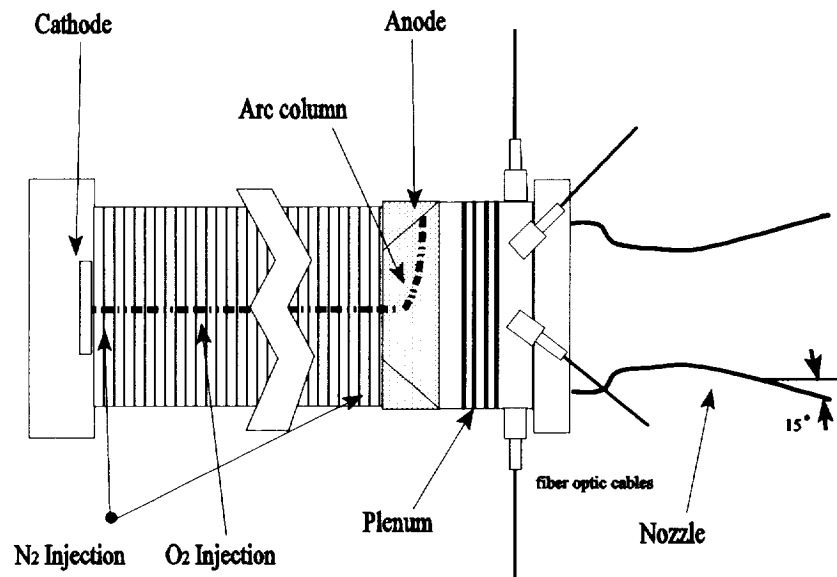


**Figure 2.4-** The design of the arc jet wind tunnel used in the present data collection. The plenum ring has been inserted next to the nozzle to insure that the measurements are not contaminated by the arc.

anode and the ring. See figure 2.5.

### 2.3 Optical fiber / lens adaptor

Due to the constraints and limitations of the plenum ring design, the fiber optic adaptor was carefully designed in the following manner. The objective was to build a part that would interface with the ring and the optical fiber as well as meet the criterion for radiation collection according to the Abel Inversion method.

The light collection orifice of the ring is approximately 3 mm in diameter, therefore, the flux is limited to a "parallel pipe" of this diameter. To obtain parallel light and maximize the signal-to-noise ratio (SNR) a 25 mm focusing ultraviolet (UV) grade fused silica lens was placed approximately 30 mm away from a UV grade fused silica window or flat. The flux was then focused onto an 800 micron aperture as in figure 2.6. The window was used to keep a constant vacuum in the heater as well as protect the lens from fouling or contamination. An optical fiber was placed directly behind the aperture so as to collect all the flux exiting the aperture. The UV grade, fused silica optical fiber has a 940 micron core diameter and a numerical aperture of 0.22. The fiber optic adaptor was built for each of the four fibers and mated to the plenum in an angular configuration. This angular configuration arose instead of a one dimensional translation due to the mechanical constraints of the plenum ring. To keep the optics clean and free of debris from the plasma a nitrogen purge line was placed in the fiber optic and lens adaptor.

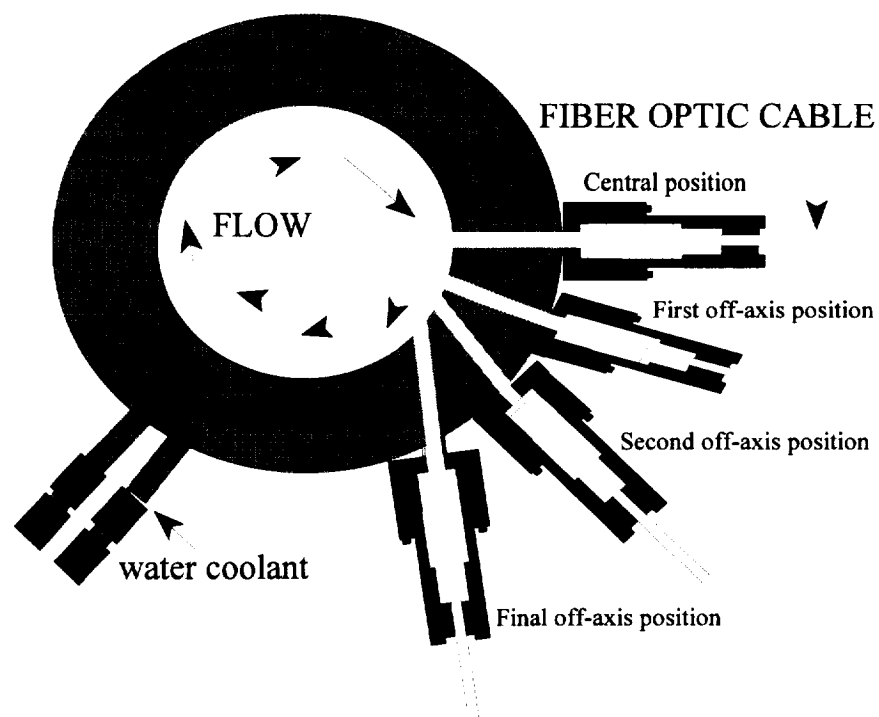
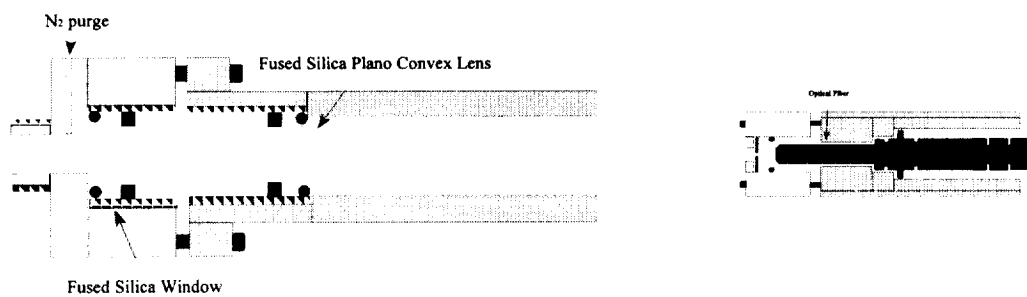
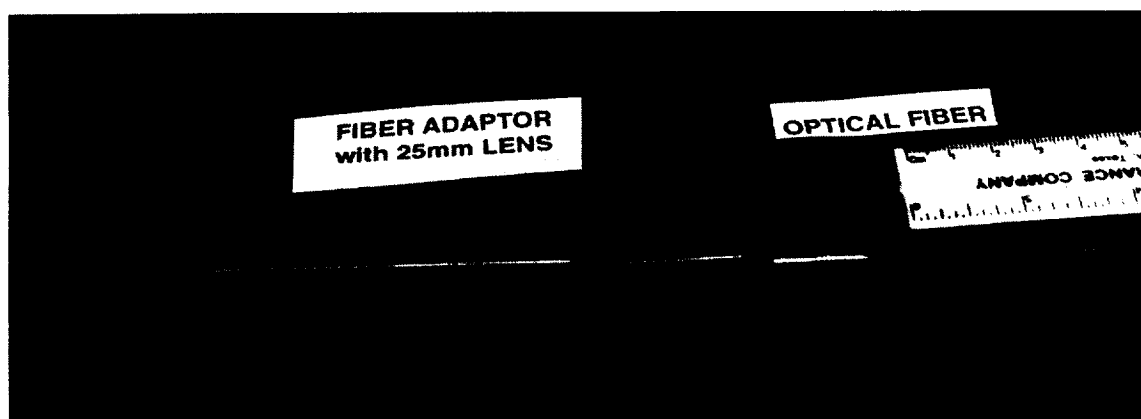


**Figure 2.5-** Optical Line of sight configuration for the plenum ring and fiber optic adaptors. (\*Note: the previous measurements were taken only from the central fiber position.)



(a)



(b)

**Figure 2.6.-** (a) Illustration and (b) actual picture of the fiber optic sensor used for collection of the spectral radiation from the plenum of an arc jet wind tunnel.



## 2.4 Spectrometers

Two spectrometers, the SPEX 270M and SPEX 1877 Triplemate, were used for spectral measurements. The following paragraphs will discuss why different spectrometers were used for this analysis. Both spectrometers are located remotely in an isolated block house (laser-room) adjacent to the arc jet wind tunnel TP2. They are equipped with a SPEX 220F fiber optic adaptor mounting kit. The mounting includes two axial adjustable collection and focusing lenses and an axial adjustable SMA type fiber optic connector. The lenses and connector slide along a railing for optimization of the light incident upon the entrance slit of the spectrometer. This mounting is also used for placement of band-pass, long-pass, and neutral density filters, in the light path.

The SPEX 270M is a single stage, 0.27 meter spectrometer designed for its high throughput and portability. All features of the 270M can be electronically controlled with either a handscan unit or with software through the RS232 ports available. It has a motor driven 2-grating turret that can be used to select either of the gratings. In this experiment gratings blazed with a resolution of 1200 l/mm and 2400 l/mm were used for spectral studies. The 270M has two exit ports that will support a photo-multiplier tube (PMT) and a linear photodiode array (PDA) detection system, which will be discussed in greater detail in the following section. The 270M was used for spectral collection that did not require fine resolution, such as atomic and vibrational bandhead line intensity.

The SPEX 1877 Triplemate spectrometer is 0.67 meter dual stage monochromator capable of efficiently filtering stray light that could otherwise alter the observed spectra. The first stage consists of two grating mounts that are motor driven and synchronized. This stage

has a bandpass that is dependent on the intermediate slit width and grating; it is 125 nm for 5 mm slit width with a 150 l/mm gratings. The next stage is consistent with normal spectrometers in that it is a Czerny-Turner system with a grating, two mirrors, exit slit, and exit ports that support PMT's and a PDA detection system. The triplemate was used for high resolution spectral data collection of the molecular spectral lines of  $\text{N}_2^+$ ,  $\text{N}_2$ , and NO. With this setup, the vibrational bandheads are very well resolved, but the rotational lines were only partially resolved.

In addition to the spectrometers, order-sorting filters were used to band-pass or band stop for the wavelengths of interest. Without these filters unwanted spectral orders could contribute to the intensity of the targeted band systems due to the grating effects of the spectrometers. Because these filters are not completely square sufficient overlapping data was collected.

## 2.5 PMT/ lock-in amplifier/ SRS data acquisition

Two separate spectrometers have been used for the reasons mentioned in the previous section as well as two different photomultiplier tubes (PMT), one on each of the two spectrometers. The Hamamatsu R955 and R943-02 PMT's were used on the SPEX 270M and Triplemate 1877, respectively.

The R955 PMT was used for its high sensitivity over a broad wavelength range, namely from 200 to 900 nanometers. This region is important for atomic excitation transitions of nitrogen and oxygen. Atomic excitation transitions tend to have high intensity in this region and therefore, the R955 at room temperature is an adequate detection source.

However, for the molecular ion transitions of nitrogen a detector with a higher signal to noise and quantum efficiency is needed. The water cooled R943-02 PMT was used with the Tripletmate spectrometer in the range from 200 to 500 nanometers. This combination of spectrometer and detector was well suited for partial resolution of the rotational band structure of  $N_2^+$  and the data is comparable in quality to previous measurements.

The data was acquired by using Stanford Research Systems lock-in amplifiers models SR510 and SR550 each controlled by a separate computer. The SR575 and SR565 lock-in software packages are used to collect and store data in binary format. The data is changed to ASCII format and imported into the Sigma Plot v.2.0 software for data analysis.

All of the data used for temperature measurements was collected with the two spectrometer systems just described. However, preliminary data was taken with a photodiode array (PDA) and optical multichannel analyzer system as will be described in the following section. The PMTs allowed only a single fiber to be collected at a time, therefore the method was time consuming and inefficient. Future recommendations for system improvement will be discussed in the following chapters.

## 2.6 Optical multichannel analyzer (OMA)

The EG&G Princeton Applied Research (PARC) OMAlII was used for preliminary testing of the plenum to find signal strengths and spectral characteristics. The OMA system consists of the model 1460 console and the EG&G PARC model 1421 gateable photodiode array (PDA).

The console controls the data acquisition, spectral display and memory storage of

files. various data acquisition modes are available as well as different scanning sequences. The scanning sequence can be live, live minus background or accumulation of intensities. In live and live minus background only 16,000 counts are attainable. However, in accumulation mode the counts are determined by the number of times scanned and duration of each scan. The console has a touch screen for easy access to the numerous options offered. It can communicate with printers, plotters or other computer through the RS232 port.

The EG&G PARC photodiode array has a 25 mm long detector surface composed of 1024 pixels or photodiode elements. The detection process involves a photoreactive release of charge from the capacitance of the detector elements. The capacitors are recharged after each exposure period. The spectral range is effective from 250 to 850 nm.

## 2.7 Experimental procedures

This chapter attempts to explain the efforts made in the laboratory. It should be used as a guideline for setting up certain equipment and taking measurements. Optical alignment, instrumentation and calibration techniques are discussed in detail so that the reader understands the work involved in pursuing these measurements. This chapter is also a precursor to the explanation and future recommendations in chapter 6. All of the laboratory work performed for this experiment took place in the arc jet facility.

### 2.7.1 Optical alignment

The arc jet wind tunnel is separated from the laboratory where all of the measurement devices are located. Therefore, as explained in some detail before, it is necessary to collect

and transport the light of the arc jet in an efficient manner. The light was collected by a highly transmissive field lens, transported by an optical fiber to a set of relay lenses mounted on the spectrometer. The relay lenses focused the light onto the entrance slit of the spectrometer. Inside the spectrometer the light passed through an optical chopper, reflected off three mirrors and a grating before reaching the exit slit. The PMT is positioned behind this exit slit and had a small photocathode area to collect the flux. This optical train presents quite a challenge for alignment and is no trivial task.

First the PMT was aligned to the spectrometer by using a monochromatic light source, a narrow slit and then measuring the output signal versus position. Once the maximum signal was reached the PMT was set into place. With the detector in place the rest of the optics could be aligned appropriately. Assuming that the relay mirrors and grating inside the spectrometer were aligned according to the factory specifications, the collecting and focusing optics outside needed to be aligned. These lenses were designed to work with a fiber optic adaptor and translated with three degrees of freedom. The fiber was installed into the mount with x, y, and z motions as well, and a monochromatic light source was positioned on the other end of the fiber. The fiber and lenses were coarsely adjusted until optimal focusing occurred on the entrance slit. Then, opening the slit the signal was read as fine adjustments were made until the signal maximized. This procedure is performed at different grating positions to ensure the system is aligned for the spread of wavelengths. The alignment of the optical chopper was purposely left out as it has a large aperture area and alignment is trivial. The chopper is mounted inside the spectrometer just after the slit.

### 2.7.2 Instrumentation and data acquisition

As noted in the previous chapter the instrumentation required for spectral measurements involved a spectrometer, photomultiplier tube, lock-in amplifier, power supplies, and data acquisition computer. The SPEX 270M spectrometer has the ability to be controlled either by a hand held operator or via an RS232 port to a computer loaded with the specific software. Because this latter option calls for a second computer the hand-scan device was mainly used for control. This device lets the user define the slit widths, scan rates, grating positions, as well as many other features.

The next objective is to optimize the phase of the lock-in amplifier (SR510). This model requires manual adjustment of the phase until a maximum signal-to-noise ratio is achieved. In addition to phase, the time constant of the lock-in is set depending on the SNR and scan rate. In our case the time constant was set to 100 milliseconds. Finally, when acquiring data the lock-in software has a maximum of 4000 data points. A sampling frequency must be chosen in accordance with the scan rate in order to collect the entire targeted spectrum. For example table 4.1 shows a typical set of conditions used for a single scan.

**Table 2.1-** Typical Parameters Used for the Lock-In Amplifier.

Scan Rate	0.2 nm/sec	0.5 nm/sec
Sample Frequency	10 Hz	5 Hz
Time Constant	0.1 sec	0.1 sec
Wavelength Range	80 nm	400 nm
Total Time	400 sec	800 sec
Total Data Points	4000	4000

The next instrument to optimize is the PMT by adjusting the voltage delivered from a stabilized power supply. The PMT has an optimum range of voltages depending on the signal delivered to its photocathode. More gain does not necessarily constitute a greater signal to noise ratio according to the specifications from the manufacturer of the PMT.

### 2.7.3 Calibration

The system used to collect spectral emission radiation from the plenum consisted of various devices with different spectral sensitivities. Therefore, correction for these different components was critical to measuring the intensities from band systems that spread across a significant range of wavelengths. The spectral data was corrected for wavelengths and intensities by carrying out wavelength and intensity calibrations.

#### 2.7.3.a Wavelength Calibration

The wavelength calibration was performed by two different methods for certainty. The first method involved using a standard low pressure mercury (Hg) lamp. The second method uses knowledge of the expected transitions of each of the species in the flow.

The spectral scans of low pressure mercury lines were obtained by each of the different systems that were used in the data collection process. Each system has a variety of components that can influence the overall spectral location of individual lines. For example, one system includes the SPEX 270M spectrometer, 1200 l/mm grating, stepping motor driver, and the SR510 lock-in amplifier. The shift in measured wavelength was calculated and the correction is applied to the spectra from the plenum. The other system was the SPEX 1877

spectrometer with a 2400 l/mm grating and the SR530 lock-in amplifier.

Known isolated emission lines were used to check that this method was accurate across the spectral range of interest. The (0,0) bandhead of  $N_2^+$  (B-X) at 391.44 nm was the primary line used in correcting for the shorter wavelengths. The nitrogen atomic lines around 820 nm were used for correction in the longer wavelength region.

### 2.7.3.b Intensity

Intensity calibration for the optical system involved using a standard tungsten ribbon filament lamp as a blackbody source. The complete detection system was calibrated, including the plenum ring aperture, optical fiber, spectrometer and photomultiplier tube as shown in figure 2.7. The filament of the tungsten lamp was imaged onto the plenum ring with a calcium fluoride lens so that it overfilled the 3 mm aperture. The emission was then collected and analyzed just as the emission from the air plasma in the plenum. The calibrated values of the tungsten lamp was given in watts per centimeter cubed per steradian ( $W/cm^3/str$ ). The following equation gives the corrected intensity ( $I_{corr}$ ),

$$I_{corr} = I_{cal} * \frac{I_{spectra}}{I_{tung}} \quad (2.1)$$

where  $I_{cal}$  is the calibrated intensity values of the lamp,  $I_{spectra}$  is the raw measured signal of the arcjet emission, and  $I_{tung}$  is the signal measured for the lamp. All are functions of wavelength.

The tungsten lamp is an ideal source for wavelengths longer than 300 nm with increasing spectral radiance at longer wavelengths. However, at shorter wavelengths a source



designed for ultraviolet emissions such as a deuterium lamp or argon mini-arc system would be preferred. These two sources were not available at the time of calibration so the tungsten lamp was extended down to 225 nm. Figure 2.8 shows the relative spectral response of the detection system.

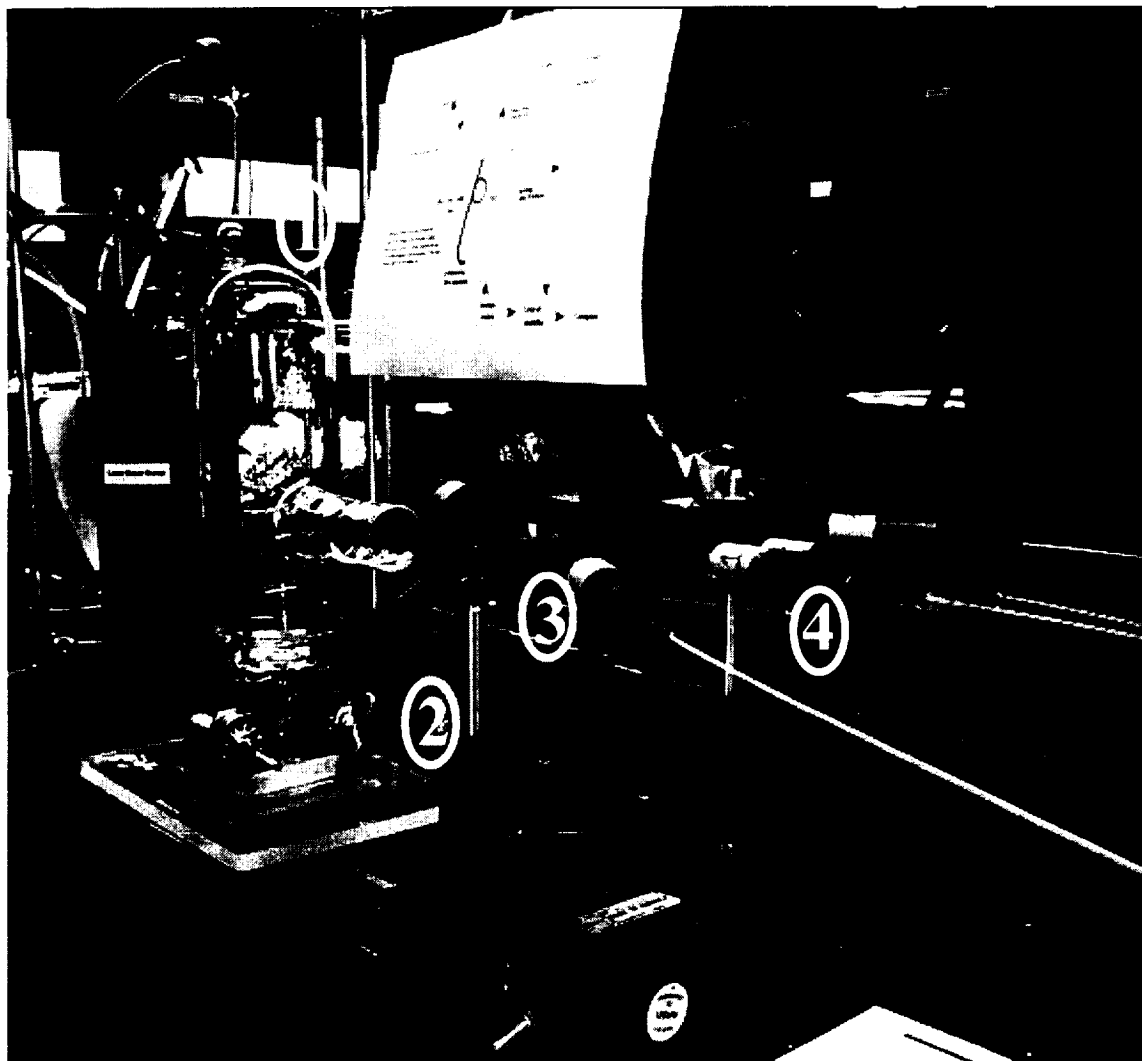


**Figure 2.7-** Experimental configuration for the intensity calibration using a standard tungsten ribbon filament lamp. The filament of the lamp was focused onto the entrance aperture of the copper ring. The numbers correspond to the following elements: 1) standard tungsten lamp; 2)  $\text{CaF}_2$  lens; 3) copper ring section; and 4) fiber assembly.

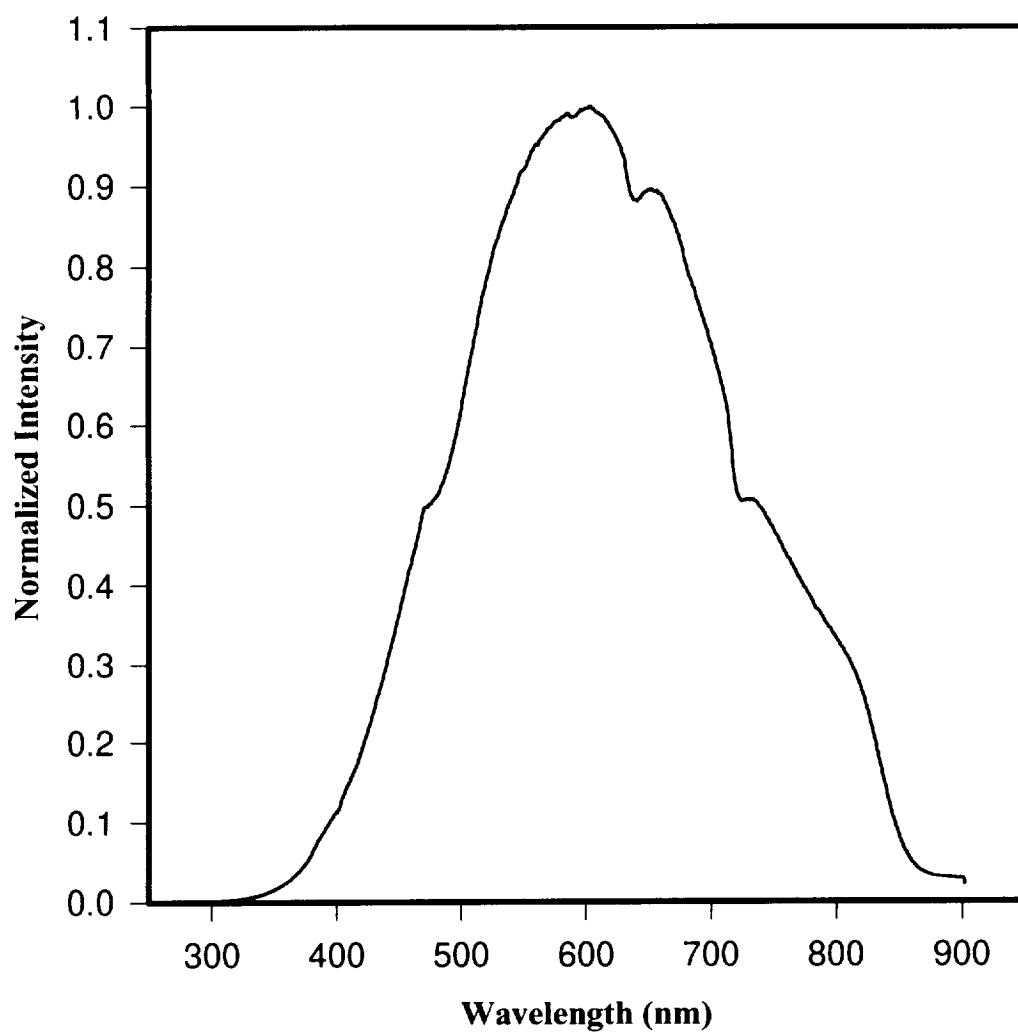


**Figure 2.8-** Relative spectral response of the SPEX 270M detection system with lenses and optical fiber over the wavelength range of interest.

## CHAPTER 3

### Theory and Background of the Radiative Air Plasma

#### 3.1 Plasma emission spectroscopy

As previously noted in Chapter One thermal air plasmas play the key role in determining the energy transfer and electron recombination effects on different TPS structures. Thermodynamic characterization of the plasma involves determination of the energy distribution and population of the species in atoms, ions, and electrons as well as the number density of these species. Due to the relatively high pressure in the plenum the present study will only involve the equilibrium state of the flow and therefore, the nonequilibrium conditions of the plasma are not considered<sup>9</sup>.

In local thermodynamic (LTE) equilibrium all involved species share common processes that contribute to their energy balance. Therefore, their velocity profiles are determined by Maxwellian velocity distributions and their radiative emissions follow that of an optically thin plasma. The only parameters that affect their distribution are temperature and pressure and it is completely determined by the Boltzmann relation. The population of any given electronic level  $n_i$  that corresponds to an energy  $E_i$  and degeneracy value of  $g_i$  is related to the ground state population  $n_o$  and its corresponding degeneracy  $g_o$  by the following:

$$\frac{n_i}{g_i} = \frac{n_o}{g_o} \exp\left(-\frac{E_i}{kT}\right) \quad (3.1)$$

where  $k$  is the Boltzmann constant and  $T$  is the equilibrium temperature. However, departures from local thermodynamic equilibrium (LTE) can occur in recombining or ionizing plasmas<sup>9</sup>. In the case of the arc jet the gases are excited to their upper energy levels and then mixed in a long cylindrical chamber where they may approach a state of equilibrium before being ejected into a large evacuated chamber. This is called the plenum and is the area of interest, therefore, all predictions of the thermodynamic state can be assumed in thermo-chemical equilibrium.

### 3.2 LTE temperature distribution in the plasma

For atmospheric or high pressure plasmas the magnitude and frequency of collisions is high enough for the free electrons to efficiently transfer their kinetic energy to heavy species. And the population of bound electronic levels is related by collisions with free electrons. This type of plasma will result in a Boltzmann type distribution at the temperature of the free electrons. When radiation escape occurs, due to the plasma extent being finite, the radiative field cannot be that of a blackbody.

As stated before the LTE temperature of a specific species is determined from the Boltzmann relation in equation 3.1. However, two factors are needed to find this temperature, the number density of the upper and ground states of the transition. By taking the natural logarithm equation 3.1 becomes:

$$\ln\left(\frac{n_g g_o}{n_g g_i}\right) = - \frac{E_i}{kT} \quad (3.2)$$

Now, the LTE temperature can be calculated from the slope of the line from the ground state to the electronic state that is to be determined. If the levels do not follow the Boltzmann relation, then they will give a non-LTE temperature and therefore be meaningless. The number density of an excited state can be determined from the emission of that radiation as long as the state spans a narrow region of the spectrum, is not overlapped by other transitions, and have enough intensity to be differentiated from the background radiation present. Therefore, only atomic electronic transitions will be considered from this plasma as the molecular transitions cover a wide range of the spectrum, are often overlapped and, in the case of rotational lines are often too weak and closely spaced to be determined by the current spectroscopy methods. However, the molecular bands have been well modelled in computer codes such as the Non-Equilibrium Air plasma code (NEQAIR)<sup>10</sup>.

The number density of a transition's upper state can be related to the calibrated intensity measured by the following equation:<sup>11</sup>

$$I \left[ \frac{W}{cm^2 \cdot str \cdot nm} \right] = \frac{hc A_u g_u N}{12.566 I Z_e} e^{-\frac{E_u}{kT}} \quad (3.3)$$

where  $A_u$  is the Einstein coefficient and the upper energy is given for  $E_u$ . Following the work of Terrazas-Salinas et al<sup>4</sup>, 1994 electronic transitions of the oxygen and nitrogen atoms were considered and are tabulated, along with their respective constants in Table 3.1.

From Equation 3.3 the electronic temperature for the oxygen and nitrogen atoms can be found by plotting the following proportionality and determining the slope of the line.

$$I_e = K \cdot \frac{A_u g_u}{I} e^{-1.439 \frac{E_u}{T_e}} \quad (3.4)$$

**Table 3.1-**Atomic Transitions Considered for the LTE Temperature Measurement of Nitrogen.

$\lambda(\text{nm})$	$A_u(10^8 \text{ s}^{-1})$	$\epsilon_u(\text{cm}^{-1})$	$g_u$	$g_l$
409.995	0.034	110522	4	2
410.996	0.04	110546	6	4
415.146	0.013	107447	4	6
421.592	0.031	106998	4	2
422.304	0.051	107039	6	6
491.49	0.0076	106479	2	2
493.503	0.0158	106479	2	4
528.118	0.0028	107039	6	6
532.87	0.0025	106871	8	6
742.36	0.052	96752	4	2
744.23	0.106	96752	4	4
746.83	0.161	96752	4	6
820.036	0.0367	95477	2	2
821.071	0.0363	95495	4	4
821.632	0.16	95533	6	6
822.312	0.202	95477	2	4
824.237	0.102	95495	4	6
856.774	0.0458	97806	4	2
859.001	0.19	97770	2	2
862.924	0.238	97806	4	4
865.587	0.099	97770	2	4
868.027	0.191	94883	8	6
868.34	0.133	94832	6	4
868.616	0.079	94795	4	2
870.326	0.171	94772	2	2
871.171	0.101	94795	4	4
871.884	0.054	94832	6	6

**Table 3.2-** Atomic Transitions Considered for the LTE Temperature Measurement of Oxygen.

$\lambda(\text{nm})$	$A_u(10^8 \text{ s}^{-1})$	$\epsilon_u(\text{cm}^{-1})$	$g_u$	$g_l$
394.73	0.0033	99095	15	5
436.83	0.0066	99680	9	3
615.73	0.0701	102865	25	15
645.5	0.071	102116	5	15
700.21	0.0325	102908	15	9
715.68	0.473	116631	5	5
725.44	0.062	102412	3	9
777.34	0.34	86629	15	5
794.93	0.373	113719	21	15
844.65	0.28	88631	9	3

This technique finds the LTE temperature of an atom by the distribution of its excited electronic levels. The Boltzmann plot will be  $I_e \lambda / A_u g_u$  versus the upper energy level of the transition  $E_u$ . The resulting slope is  $-1.439/T_e$ . The calibrated intensity was measured across the line of sight of the plasma resulting in an integrated quantity of the emissions. The inverse of this process is of more importance when characterizing the volumetric plasma field flow. This inverse is called the Abel Inversion and will be discussed in the following sections. The electronic temperature will be calculated from the Boltzmann plots only after the radial intensities are obtained from the Abel inversion.



### 3.3 Molecular properties

#### 3.3.1 Vibrational temperature

The emission spectrum of the arc jet is composed of many band systems that can help determine the distribution of the vibrational populations. The band systems most predominate in the flow are the  $N_2^+$  first negative,  $N_2$  second positive, and NO  $\beta$  systems. The strongest NO bands occur in the spectral region from 200-280 nm and originate from ground state vibrational levels. Because the intensity from the spectrum is much lower compared to the higher wavelength regions, little information about the vibrational distributions can be obtained from these bands. Table 3.3 provides the strongest vibrational transitions measured.

**Table 3.3-** Strong Vibrational Bands in the Air Plasma

$N_2^+$ (First negative system) $B^2 \Sigma_u^+ - X^2 \Sigma_g^+$		$N_2$ (Second positive system) $C^3 \Pi_u - B^3 \Pi_g$		NO ( $\beta$ system) $B^2 \Pi - X^2 \Pi$	
Band ( $v'-v''$ )	Band Origin (nm)	Band ( $v'-v''$ )	Band Origin (nm)	Band ( $v'-v''$ )	Band Origin (nm)
0, 1	427.81	0, 1	357.69	1, 4	255.79
1, 2	423.65	1, 2	353.67	3, 4	243.3
2, 3	419.91	2, 3	350.05	3, 3	233.14
3, 4	416.68	0, 0	337.13		
0, 0	391.44	1, 0	315.93		
1, 0	358.21	2, 1	313.6		
2, 1	356.39	2, 0	297.68		
3, 2	354.89				
4, 3	353.83				
2, 0	330.8				

Selecting the bandheads for temperature determination involves choosing those transitions that are isolated from other transitions. However, in the regions of interest for the vibrational bandheads from different species all three of the above can contribute to the emission at a single band of wavelengths. Therefore, it is important to choose a model that accurately predicts the spectral emission of overlapping band systems.

Two different computer codes are used in determining the spectral parameters. The NEQAIR, non-equilibrium air flow code is used to fit the collected data. The code is normally modified when looking at specific data because different sets of conditions can cause perturbations in the spectra. Perturbations in all wavelength regions have not been thoroughly modeled as there is not experimental data supporting all conditions. The perturbations occur when the potential curves of a species electronic states cross and they cause what seem to be extraneous lines or dips in the spectra. This affects the normal spacing of lines and must be taken in consideration when spectral fitting.

### 3.3.2 Rotational temperature

Measurements for vibrational and rotational temperatures for the same species, under LTE conditions, will be equal to each other within the accuracy of the measuring device. However, for all practical purposes it is extremely difficult to determine this temperature due to factors like: overlapping bands, low intensity, and resolution. It would be most interesting to measure the emission from rotational bands that are not overlapping with other species in the flow. This is difficult due to overlap of the strong bands of  $N_2^+$ (first negative),  $N_2$ (second positive), and NO(gamma bands) in the wavelength range from 200 to 450 nm. The next

obstacle to experimentally determining rotational temperatures is the resolution of the bands. In most cases the bands are quite narrow and difficult to resolve with the spectroscopic methods used here in this experiment. The codes mentioned earlier can simulate this by using proper slit functions.

Another way to extract the rotational temperature is under investigation using a technique developed by M. Akundi<sup>13</sup> that analytically separates the P and R branch contribution and allows one to obtain rotational Boltzmann plots of the P and R branches even when they overlap. This is beyond the scope of this thesis, however, once it is completely developed the overlapping band systems could be extracted and evaluated as individual systems even with poor resolution.

### 3.4 Abel inversion method

The spectroscopic emission data taken in this experimental study was taken at four points across the plenum of the arc jet by line-of-sight measurements. This technique results in an integration of the line strengths of the individual species across the flow and is of little help in determining the LTE properties of the plasma. Thus, we use the Abel inversion to convert the data from line-of-sight( $x, y$ ) to radial coordinates ( $r, \theta$ ),. And the thermodynamic properties of the flow that will be presented in following chapter will result from the method of the Abel inversion. This technique transforms the coordinate space of the data from the line-of-sight ( $x, y$ ) to the radial positions by the following:

$$I(x) = 2 \int_r^R \frac{r \varepsilon(r)}{\sqrt{r^2 - x^2}} dr \quad (3.5)$$

where the intensity  $I(x)$ , taken from the line-of-sight, is related to the radial emission coefficient  $\varepsilon(r)$ .

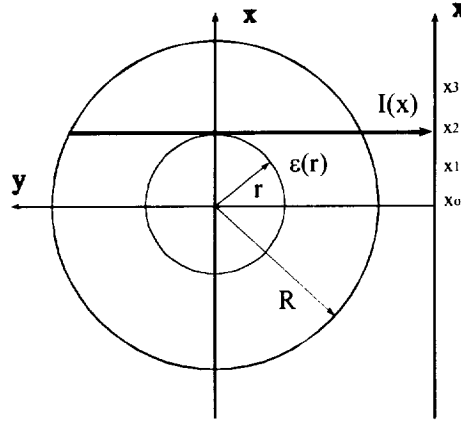


**Figure 3.1** The Abel diagram for conversion of line-of-sight emission intensities  $I(x)$  to radial emission coefficients  $\varepsilon(r)$ .

Now, by taking the Abel transform of Equation 3.5, the radial emission can be found by:

$$\varepsilon(r) = \frac{1}{\pi} \int_r^R \frac{I'(x)}{\sqrt{x^2 - r^2}} dx \quad (3.6)$$

where  $I'(x)$  is the derivative of measured intensity with respect to  $x$ . This result leads to

measurements that are very sensitive to noise in the emission and tend to greatly amplify the noise term. According to Laux<sup>10</sup>, this noise term is extremely difficult to quantify and, therefore, to model. For this reason Laux et al employed a FORTRAN computer code called the POLAB4 to Abel invert as well as quantify the error propagation of the spectral data. This code was derived from the method of Abel inversion by Owano<sup>12</sup>. This method consists of fitting the line-of-sight data to a polynomial of degree up to nine. However, with only four data points and a symmetrical function the highest degree polynomial that can be fit is degree six.

$$I(x) = a_0 + a_1 x^2 + a_2 x^4 + a_3 x^6 \quad (3.7)$$

The centerline of the plasma must have a slope of zero to be considered axisymmetric and the last radial position given by the code must have intensity equal to zero to satisfy the boundary conditions. This method was employed for several different reasons: first, the data is well fitted by the polynomials, so lengthy curve fitting does not apply; second, the polynomials are quickly fit by the computer; and third the polynomials can be transformed analytically so that the uncertainty analysis could be quantified. This latter does not apply in this case because a measurement of the standard deviation must be input into the equation in order to have a meaningful uncertainty analysis. The experimental conditions did not warrant such data because of lengthy data collection times.

## Chapter 4

### Results and Discussion

The atomic emission of nitrogen and oxygen will first be analyzed. A radial profile of electronic excitation temperature ( $T_e$ ) of the plasma is determined by using the Boltzmann plot technique for upper energy level atoms. Then, comparisons between NEQAIR 2 and experimental vibrational data will be shown as well as radial profile of  $T_v$  will be presented.

#### 4.1 Temperature determination of excited electronic states

As discussed before, the calibrated data was Abel inverted by the POLAB 4 code. At first, the four positions were used to find the function that gave a best curve fit. However, two problems arose from this transformation. In the central and 1.27-cm off-axis positions of measurement the spectra almost completely match and there is very little difference between atomic line strengths. The same is true between the 2.54-cm and 3.81-cm off-axis positions. When the peak intensities are plotted versus their radial position a "step" function results. Secondly, because POLAB uses polynomials to fit the desired plotted points, a maximum of a third order polynomial can confidently be used on the four point data. It should also be noted that at the central position a constraint is placed on the polynomial to have slope of zero for a symmetrical plasma. Another constraint of the polynomial is that the boundary condition must be zero. Many attempts were made to fit this "step" function to a third order polynomial. No satisfactory fit could be found as might be expected. Therefore,

a set of intermediate points were developed by linearly interpolating the data. Between the central and 1.27-cm position as many as four points were interpolated as well as one point between the 2.54-cm and 3.81-cm positions. Together, all nine points were collected and fit to a polynomial of degree eight.

Figure 4.1 shows the complete calibrated spectrum that was taken for finding the atomic transitions at all four positions across the flow of the plenum. There seems to be little contribution of the atomic species at the two farthest positions indicating that the temperature in that region is much lower than at the center. Figure 4.2 represents the Abel inverted spectra to show the difference between the line-of-sight spectra and the spectra that is calculated in radial coordinates from POLAB.

From Equation 3.4 a plot of  $\ln[I_e\lambda/A_u g_u]$  versus the upper energy level  $E_u$  will result in a straight line whose slope is inversely proportional to the temperature  $T_e$ . Figure 4.3a plots the Boltzmann distribution for the oxygen atomic transitions. From these points a best fit linear regression is plotted and the slope is determined. Caution should be taken when interpreting these results as the temperature measurement is extremely sensitive to changes in the slope of the fit line.

The transition plots do not represent the complete set of atomic lines collected. There are many multiplets that require much higher resolution than available in these experiments. If the multiplets cannot be separated into individual lines or if their contribution to the peak intensity is not accurately known, then they cannot be used for temperature analysis. However, from Laux<sup>6</sup> the total line intensity of the oxygen triplet at 777.3nm can be measured if the entire energy envelope is captured including the wings by using a trapezoidal slit

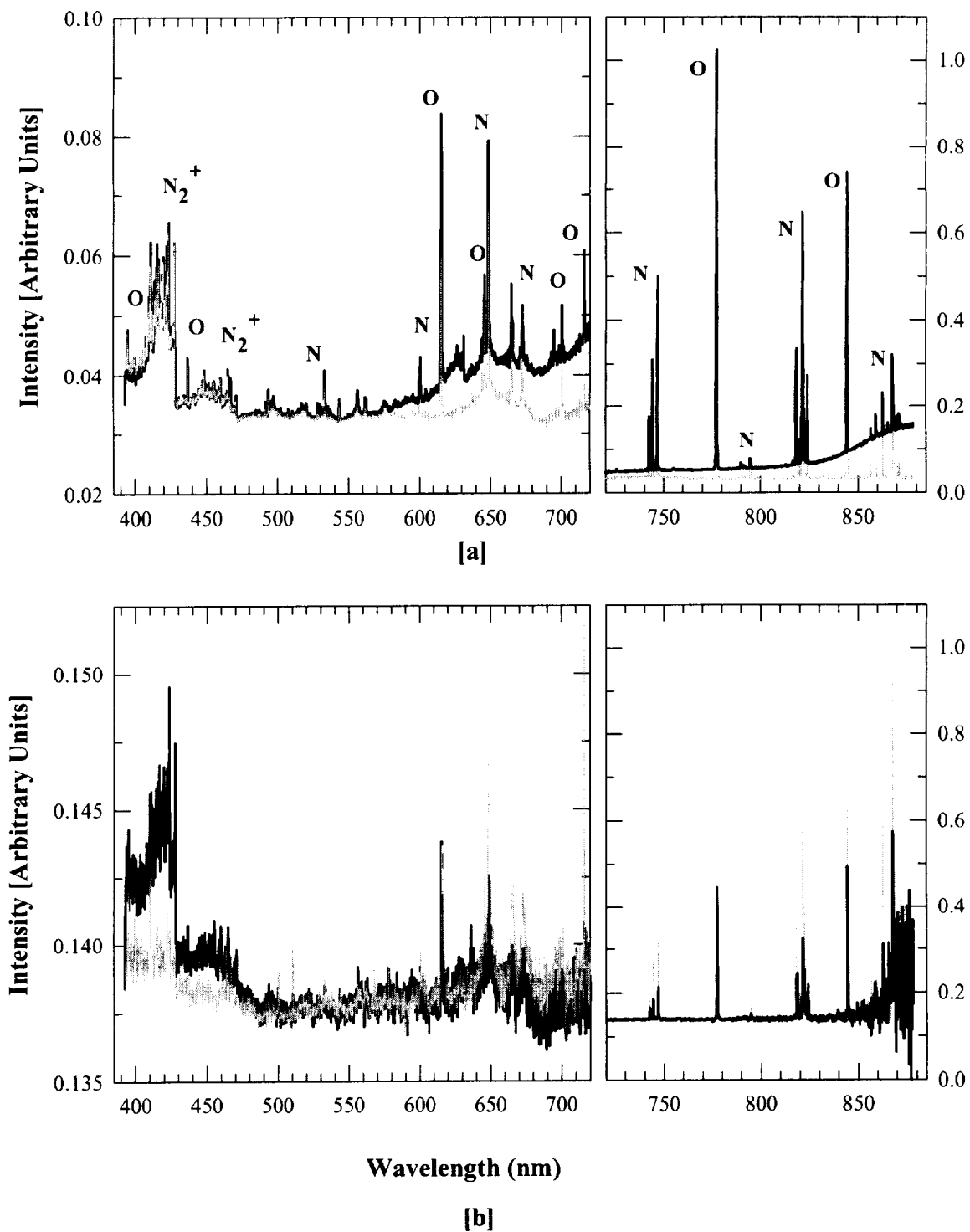


**Figure 4.1-** Experimental emission spectra of the plenum air plasma. [a] central (black) and 1.27cm (gray) line-of-sight positions. [b] 2.54 (black) and 3.81cm (gray) positions. Emission from oxygen(O), nitrogen(N) and molecular nitrogen( $N_2^+$ ) is shown.



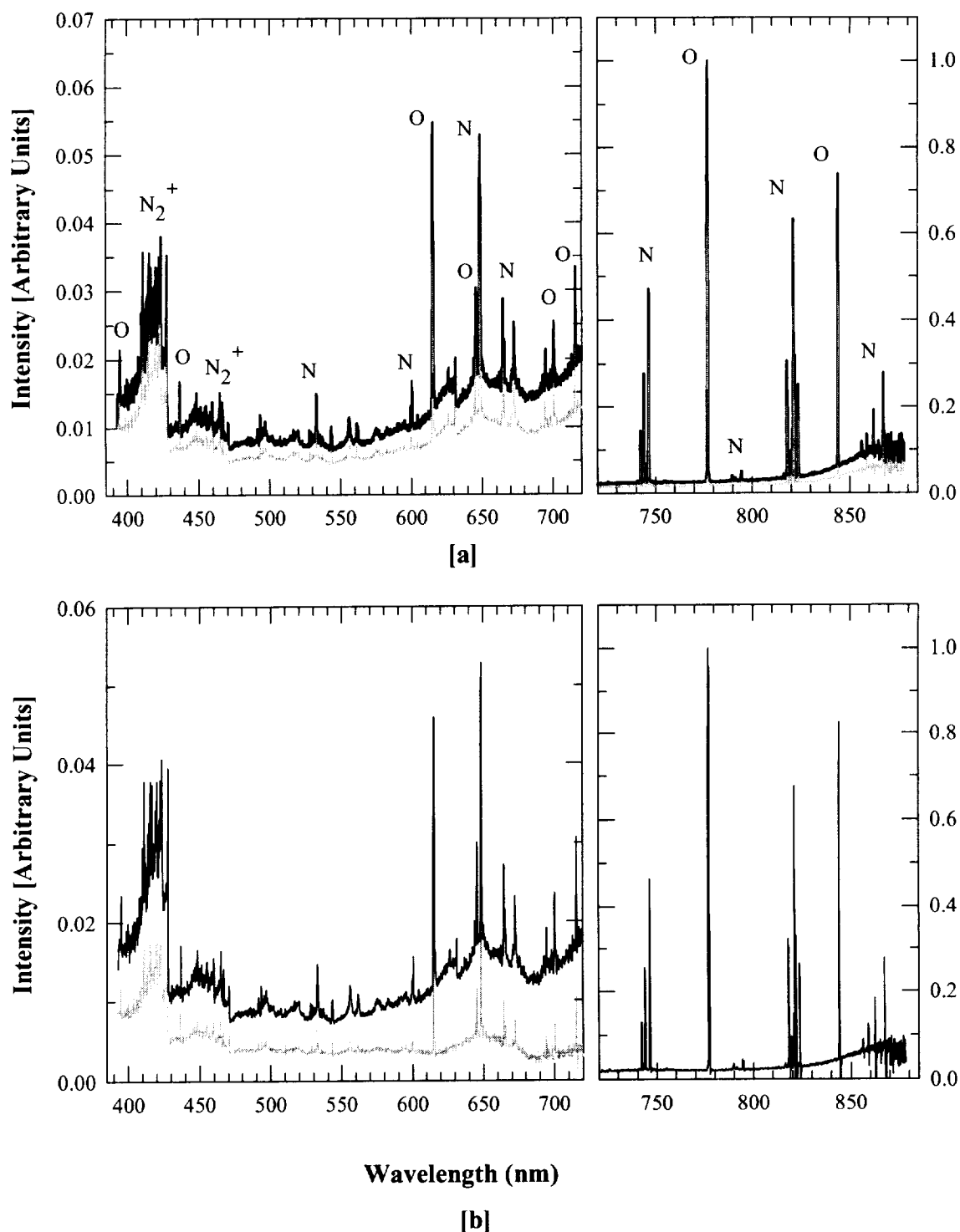


**Figure 4.2-** Abel inverted spectra of the plenum air plasma. [a] central (black) and 1.27 cm (gray) line-of-sight positions. [b] 2.54 (black) and 3.81 cm (gray) positions. Emission from oxygen(O), nitrogen(N) and molecular nitrogen( $N_2^+$ ) is shown.

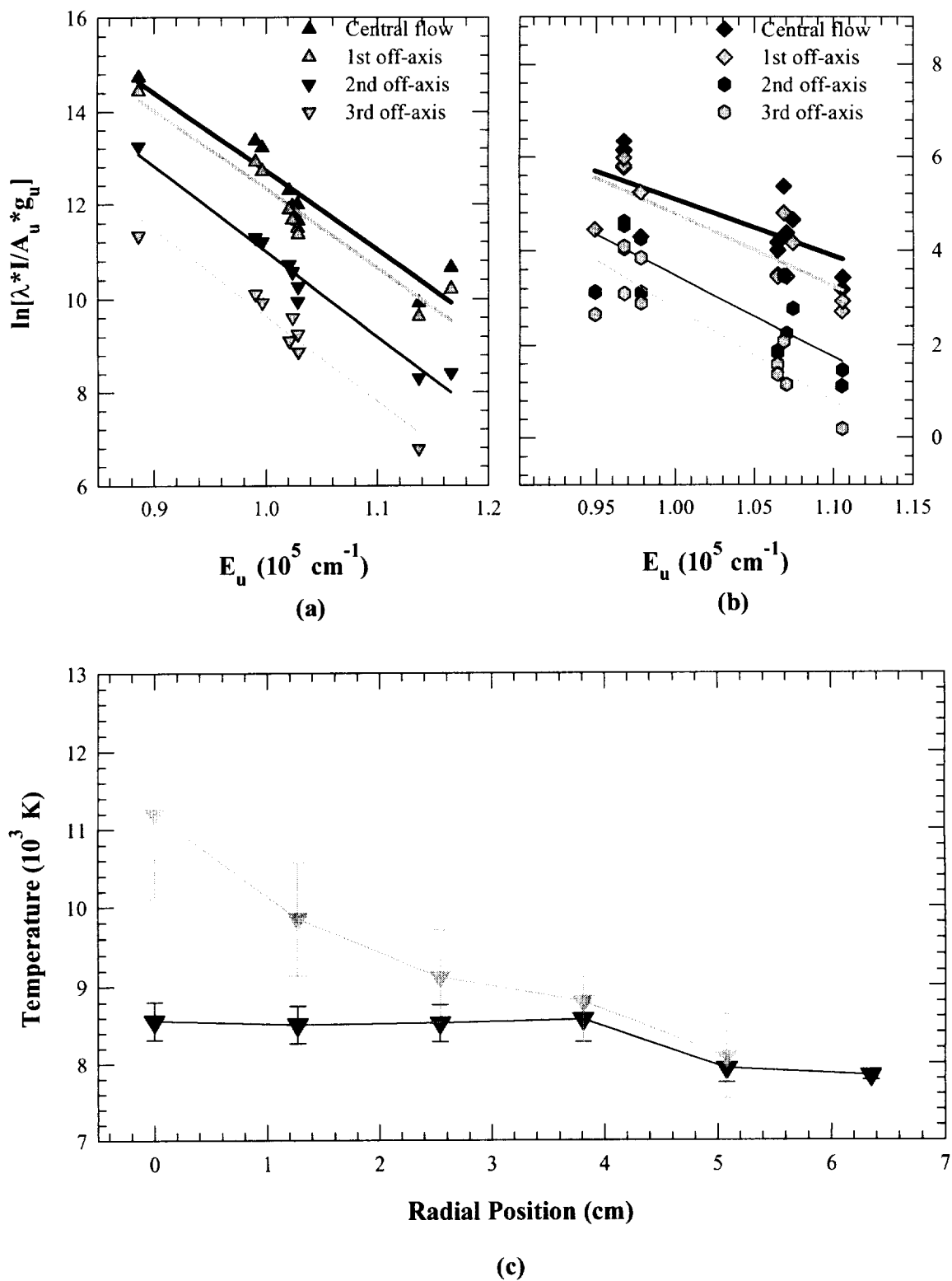


**Figure 4.3-** Boltzmann distribution for (a) oxygen and (b) nitrogen in the plenum air plasma, (c) Radial temperature profile of Oxygen (black) and nitrogen (gray).

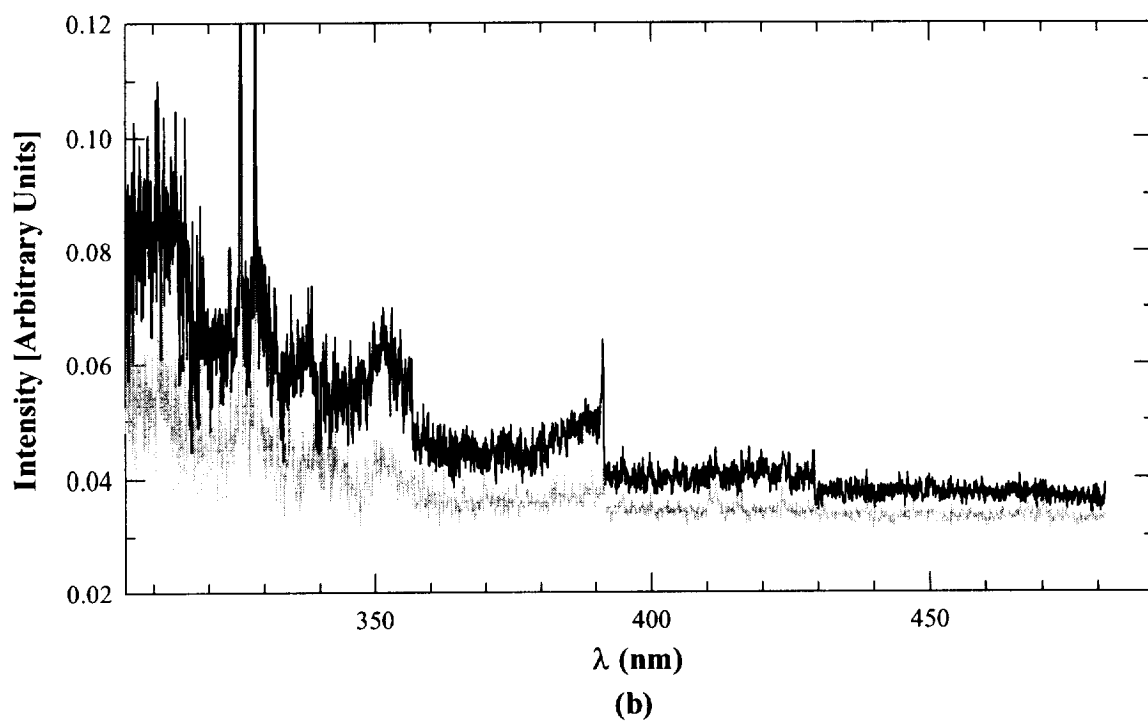
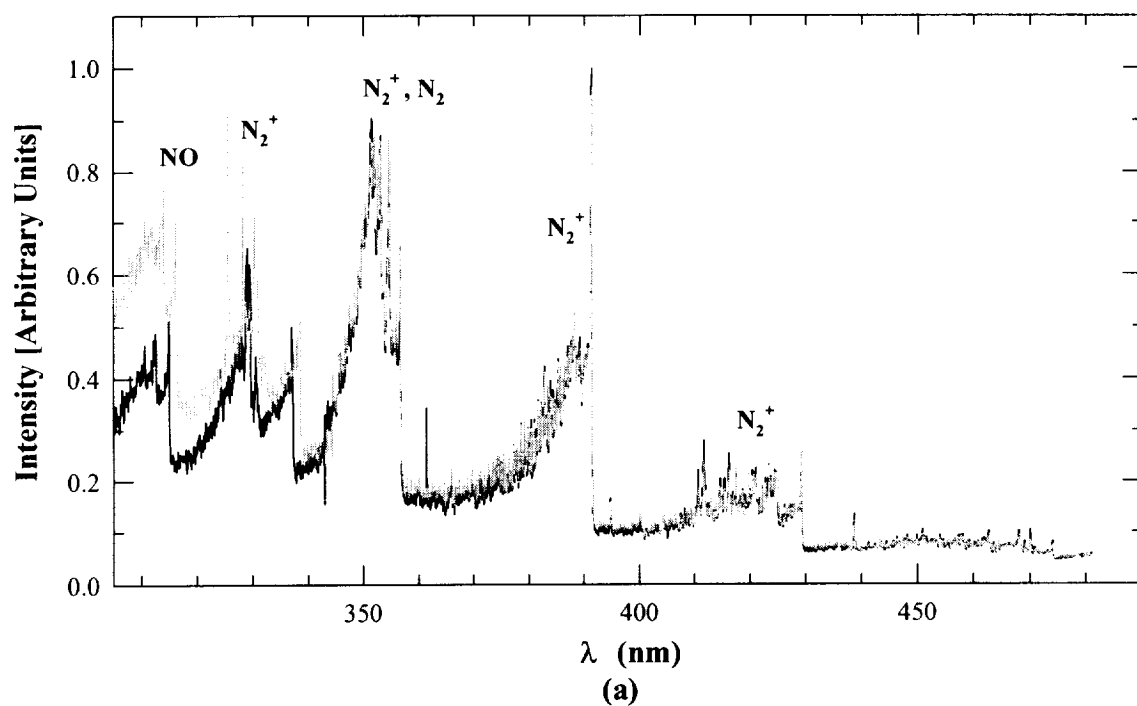
function. This could be helpful for future work, however, no measurements were made in this experiment.

Figure 4.3b shows the temperature plotted versus the radial position of the plasma as well as the error bars calculated from the Boltzmann plot. Due to the limitations placed on the Abel inversion, as previously discussed, the results of the temperature of the flow in the central position is not as meaningful as those radial positions following from 1/2" out to the border. The farthest measured spectra are also not as accurate or meaningful because they fall outside the sensitivity of the detector. Therefore, where appropriate, only the mid-flow radial profile is shown.

#### 4.2 Temperature determination of the vibrational bandheads of $N_2^+$

As shown in the previous chapter the emission spectrum of the arc jet's plenum chamber is composed of numerous band systems. Equally numerous are the possibilities for a vibrational band population measurement. However, due to the propagational error in the calibration for short wavelengths, a fit across the entire spectrum is invalid. Many attempts were made to fit the data to the NEQAIR 2 code and this is where it was determined that a calibration error could have been made<sup>14</sup>. Further investigation of the calibration technique concluded that relative comparisons between the short and longer wavelengths would have little meaning. Thus, until further improvements are made for calibration, only small spectral portions are used for data analysis.

Figure 4.4 shows the vibrational data collected with the current calibration used. The calibration should be much more accurate toward longer wavelengths since the tungsten



**Figure 4.4.-** Experimental emission spectra showing the vibrational bands of  $\text{N}_2^+$  (first positive),  $\text{N}_2$  (second positive), and NO; (a) central (black) and 1.27 cm off-axis (gray) and; (b) 2.54 (black) and 3.81 cm (gray) off-axis positions.

source has higher radiance and therefore increased signal to noise ratio at longer wavelengths. As a result a higher temperature source radiating more efficiently in the near UV should be used below 400nm and the overlap from 350nm to 400nm by a tungsten source should be compared for a more accurate calibration. Also, a  $\text{CaF}_2$  lens was used to image the tungsten source onto the entrance aperture of the plenum ring which will result in errors in absolute calibration. The lens was used to attempt to collect flux from the filament only and reduce the outside background intensity. Stray or reflected light could cause erroneous measurements in the calibration technique.

The Abel inverted spectra taken from the collected and the linear interpolated data is shown in figure 4.5. As discussed previously five linear interpolated data points were added to the four sets of spectra taken and a seventh degree polynomial was used to invert the data for the radial positions. A radial vibrational temperature profile was obtained from a Boltzmann plot of the Abel-inverted intensities of the  $\text{N}_2^+$  first negative (2-1) and (1-0) band heads at 356.1 and 357.9 nm, respectively, using a technique similar to Ref. 6. This pair of vibrational bands was selected for two reasons. First, the close spectral spacing between these two band heads ensured that potential inaccuracies in the measured spectral response (calibration) of the detection system would have minimal impact on the resulting vibrational temperature. Second, unlike many other bands of the  $\text{N}_2^+$  first positive system, the band heads of these two transitions are not affected by perturbations.<sup>10</sup> The resulting vibrational temperature profile is presented in Figure 4.6.

As mentioned earlier, emission spectra were measured at 4 lateral locations (0, 1.27, 2.54, and 3.81-cm) from 300 to 480 nm, a spectral region wherein lie many prominent bands

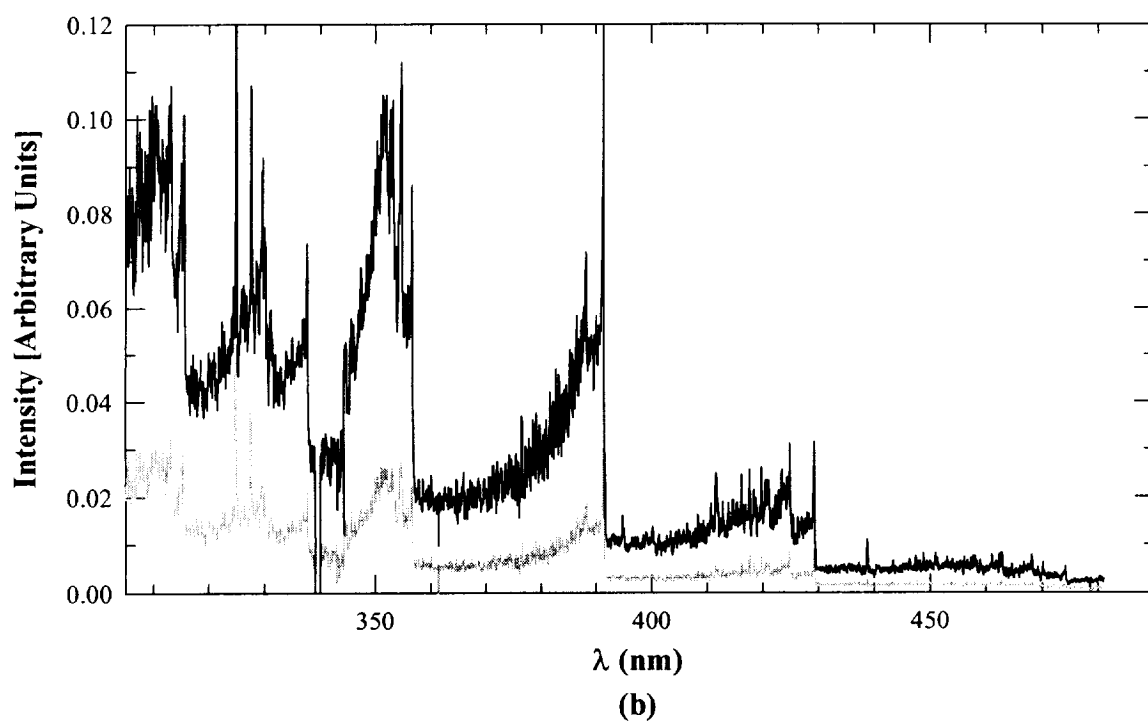
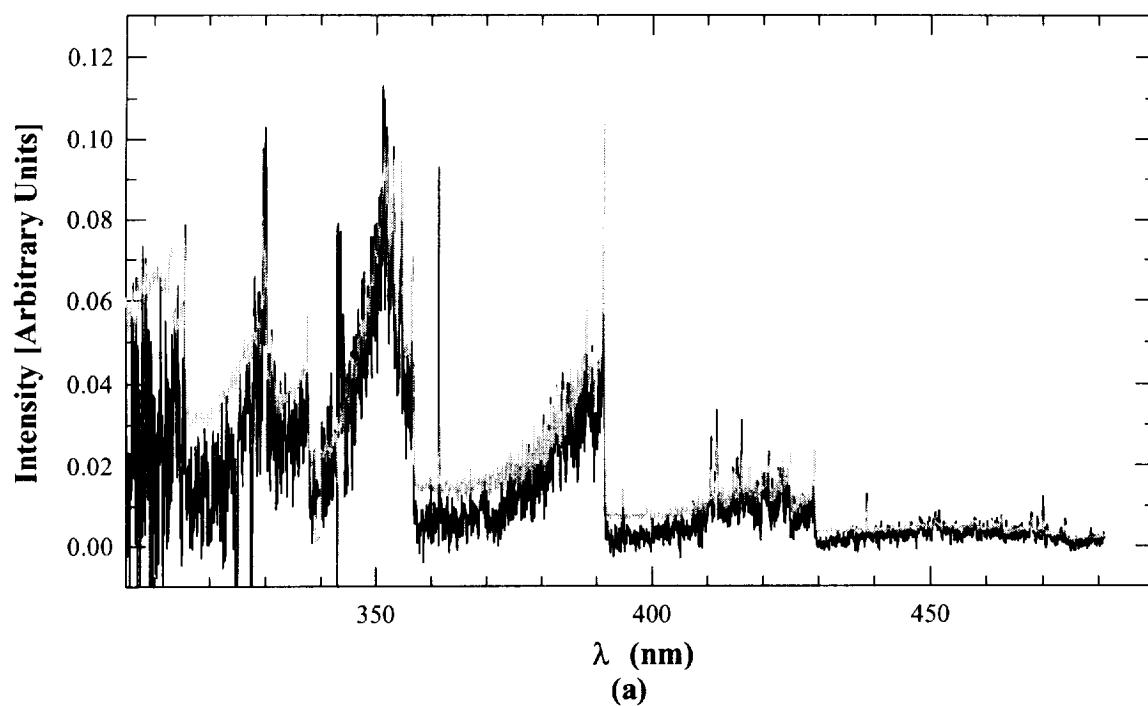


**Figure 4.5.-** Abel inversion spectra of the vibrational bands of  $\text{N}_2^+$  (first negative),  $\text{N}_2$  (second positive) and NO; (a) central (black) and 1.27 cm off-axis (gray) and; (b) 2 (black) and 3.81 cm (gray) off-axis positions.

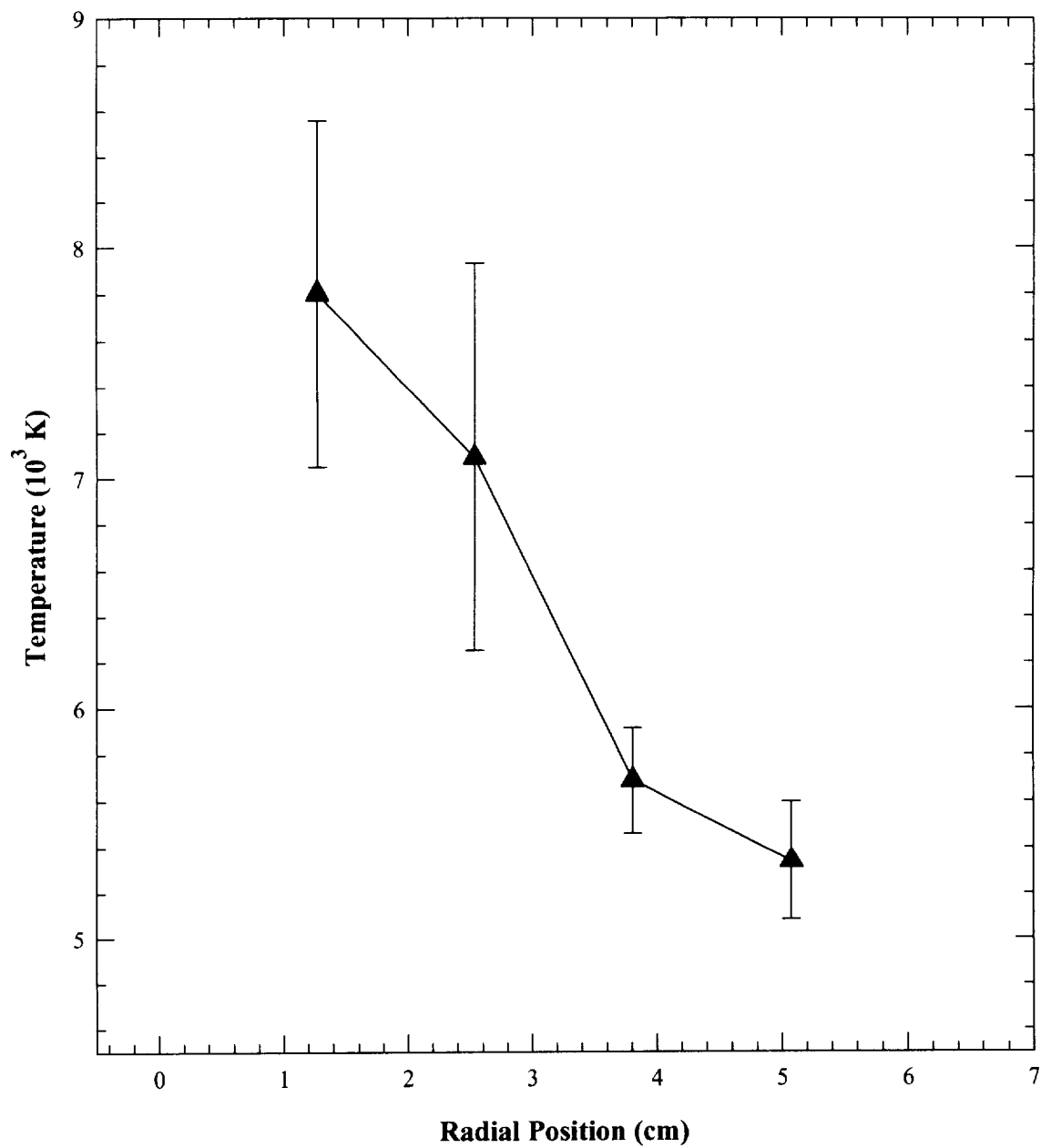


**Figure 4.6.-** Radial vibrational temperature profile of  $N_2^+$  first negative (2-1) and (1-0) band heads.

of the  $N_2^+$  first negative (1-) and  $N_2$  second positive (2+) systems. These spectra were then Abel- inverted using the program POLAB4<sup>10</sup>. The Abel-inverted spectrum at a radius of 2.54-cm is compared in Figure 4.7 with numerical simulations made with the NEQAIR2 code<sup>10</sup> for equilibrium conditions at 6500, 7000, and 7500 K. These three temperatures were chosen so as to bracket the vibrational temperature measured at a radius of 1-inch.

As can be seen in Figure 4.7, while the measured and simulated spectra agree very well above 400 nm, differences of up to a factor  $\sim 2$  are observed at shorter wavelengths. While these differences could in principle be due to nonequilibrium effects, it is shown below that they are instead more likely caused by uncertainties in the spectral calibration of the data. This conclusion is based on a comparison between measured and theoretical branching ratios for a variety of  $N_2^+$  transitions in the spectral range 330 - 470 nm. The bandheads from a given vibrational level  $v'$  should have intensities in the ratios  $A_{v'v''} \Delta E_{v'v''}$ , where  $A_{v'v''}$  is the band Einstein emission coefficient and  $E_{v'v''}$  the energy difference between the upper and lower states of the transition. Listed (in Table 4.1) are the measured bandhead intensities of vibrational transitions of  $N_2^+$  issued from; the  $v'=0$  state [(0-0), (0-1), and (0-2)], the  $v'=1$  state [(1-0), (1-1), and (1-2)], and from  $v'=2$  [(2-0), (2-1) and (2-3)]. Within each of these three groups of bands, the intensities were normalized to the intensity of the band closest to 420 nm. The normalized intensities are listed in the column labeled "measured branching ratios". Also listed in Table 4.1 are the Einstein  $A_{v'v''}$  and transition energies  $E_{v'v''}$  for each of these bands (from ref. 8), as well as the resulting theoretical branching ratios.

The ratio between the measured and theoretical branching ratios should be close to unity. However, as shown in Figure 4.8, they deviate by up to a factor  $\sim 2$  at short



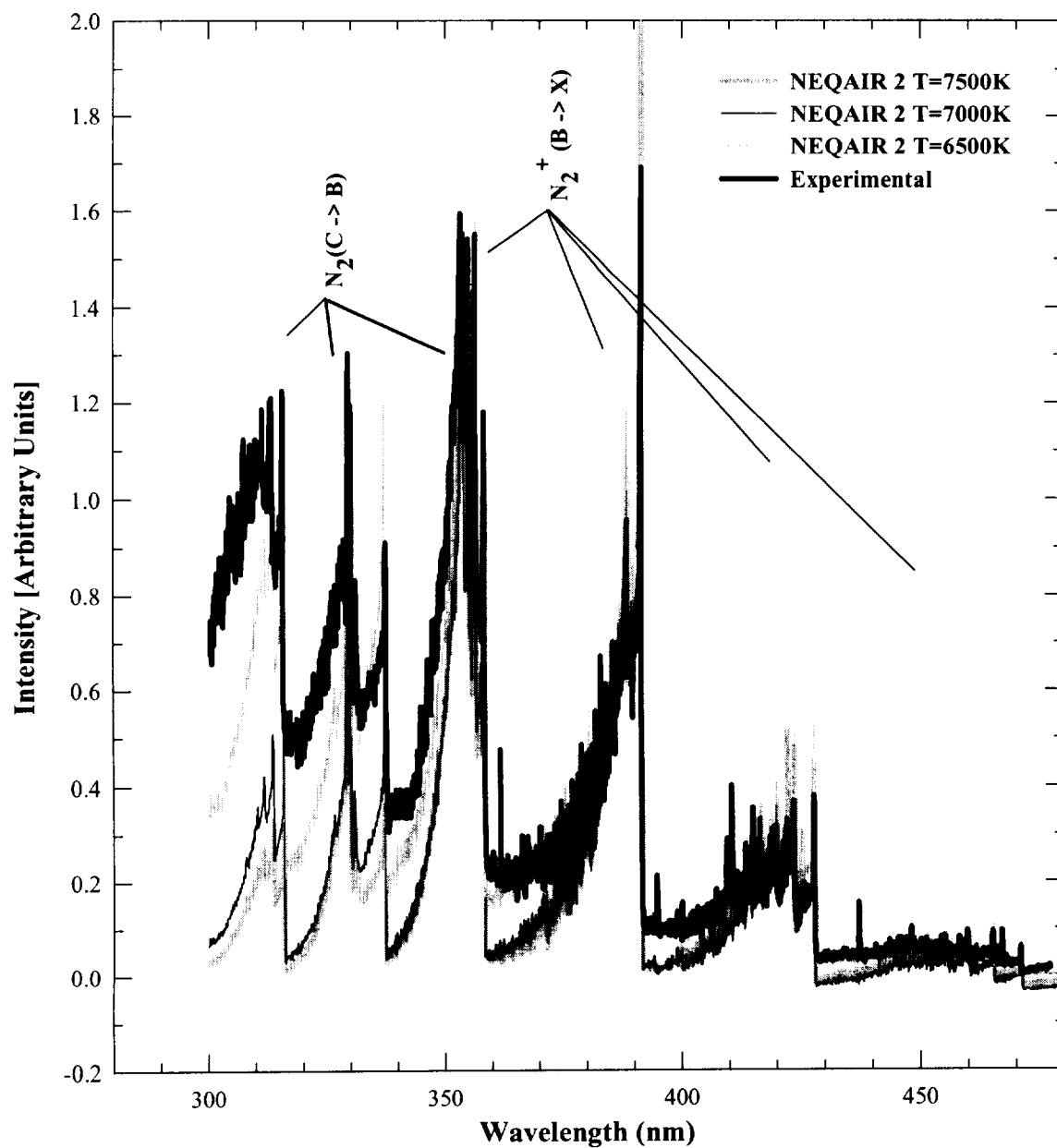


**Figure 4.7.-** Comparison of experimental and computed (NEQAIR) molecular nitrogen spectra of the plenum air plasma. The experimental spectra is Abel inverted for the 1.27cm line-of-sight position.

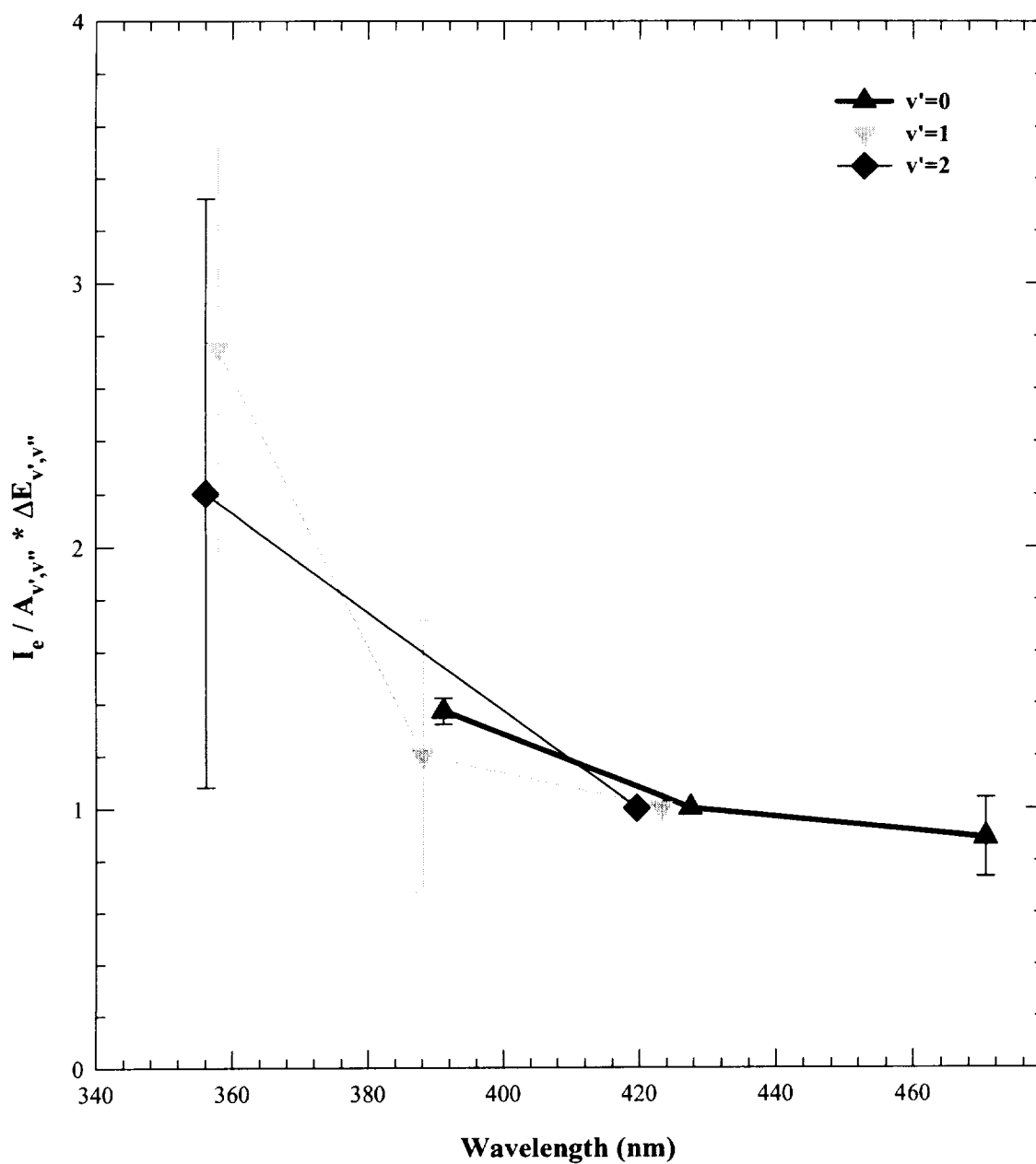


**Figure 4.8.-** Ratio of the intensity of various bandheads plotted against the product of A and  $\Delta E$  to show the estimated calibration error across the spectrum.

wavelengths<sup>15</sup>. This deviation from unity is indicative of the uncertainty in the experimental calibration. As a result, the measured spectrum shown in Figure 4.7 should be divided by the corresponding ratio. Clearly, much better agreement would then be obtained throughout the entire spectral range with the equilibrium spectral calculation at 7000 K. Therefore, the measurements are consistent with the assumption of approximate equilibrium in the central region of the plenum at least. While more work is required to improve the accuracy of the calibration below 400 nm, the above conclusion is reinforced by examining narrow spectral ranges (wherein calibration errors are minimal). Indeed, as shown in Figure 4.9, the measured vibrational temperature of  $\sim 7000$  K at  $r = 2.54$ -cm also yields the best agreement for the relative intensities of various  $N_2^+$  (1-) and  $N_2$  (2+) bands.

**Table 4.1**-Measured (exp) and Theoretical (th) branching ratios (br) for the  $N_2^+$  First Negative band system. (The product  $A_{v',v''} \cdot T_{v',v''}$  is arbitrarily normalized.)

$v', v''$	$\lambda$ (nm)	$A_{v',v''}(10^6)$	$\Delta E_{v',v''}$	$br_{th}$	$br_{exp}$
0, 0	391.44	12.19	25566	3.39	5
0, 1	427.81	3.918	23391	1	1
0, 2	470.6	0.8136	21249	0.19	.18
1, 0	358.21	6.334	27397.8	1.63	4.35
1, 1	388.1	4.257	25763	1.03	1.3
1, 2	423.65	4.522	23620	1	1
2, 0	330.8	1.033	30256	0.36	2.35
2, 1	356.39	8.61	28082	2.75	7.97
2, 3	419.91	3.69	23830	1	1

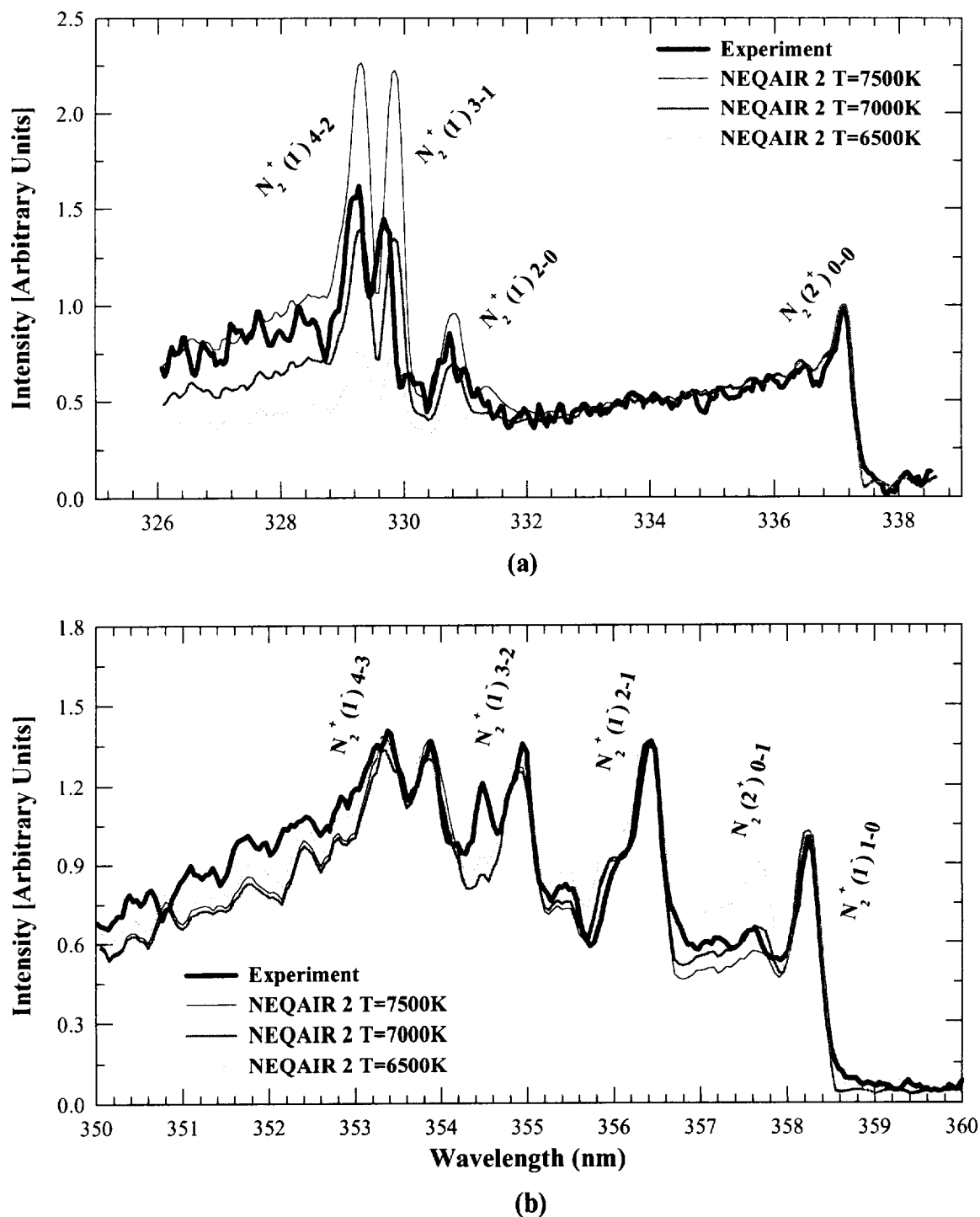
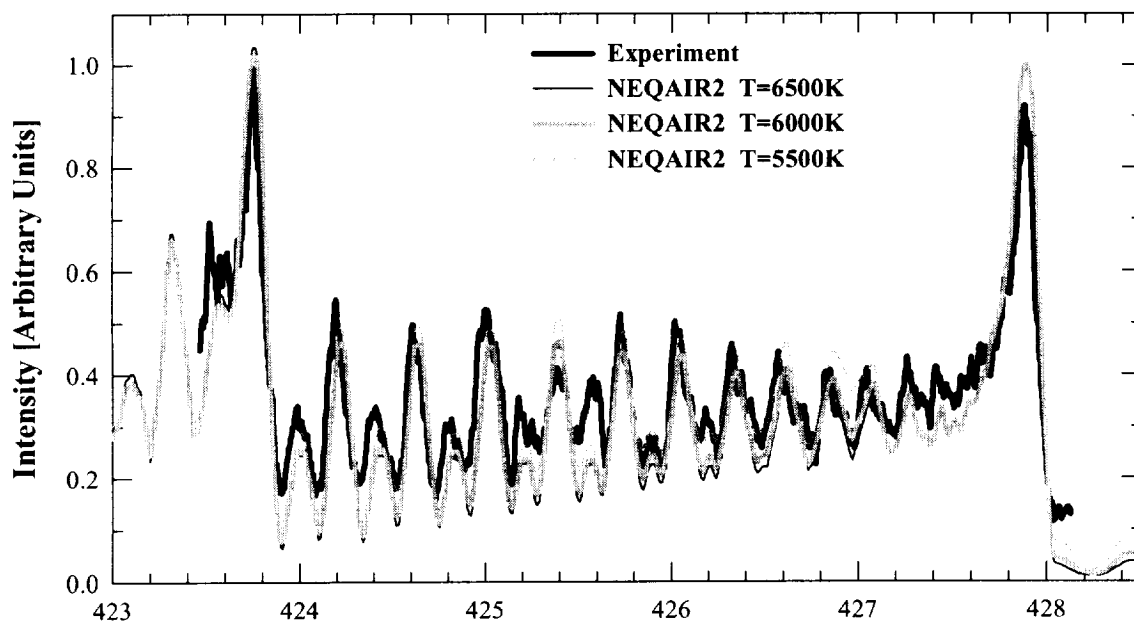


**Figure 4.9.-** Experimental and computed nitrogen spectra of the plenum air plasma. [a]  $N_2^+$  (First negative system,  $\Delta v=2$ ) and  $N_2$  (Second positive system,  $\Delta v=0$ ). [b]  $N_2^+$  (First negative system,  $\Delta v=1$ ) and  $N_2$  (Second positive system,  $\Delta v=-1$ ).

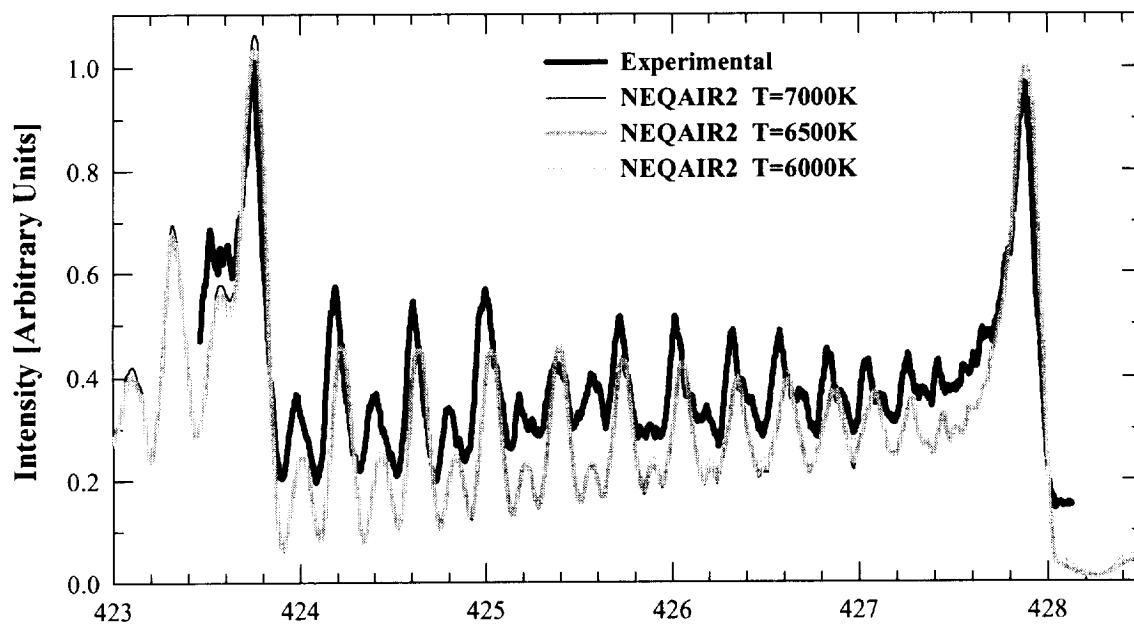
#### 4.3 Rotational temperature determination of the 0-1 band of $N_2^+$ (first negative)

Analysis of the rotational band structure of the 0-1 band of  $N_2^+$  was attempted by spectrally fitting the experimental measurements to the computed NEQAIR2 code. The comparison proved to be difficult due to several factors, including the low resolution of the data. The P and R branches are not well separated and one does not know what percentage the individual branches contribute. Figure 10 and 11 show the experimental rotational structure of the 0-1 band of  $N_2^+$  as well as the computed, best fit spectra. This method will only find rotational temperature with an error of equal to or greater than fifteen percent.

Another difficulty in finding rotational temperatures is due to the insensitivity of the Boltzmann equations. The rotational Boltzmann fractions are given as  $(3/T_r) \cdot \exp(-3J(J+1)/T_r)$ . Whereas, the vibrational and electronic fractions are given respectively as:  $(1 - \exp[-3000/T_v]) \cdot \exp(-3000v/T_v)$  and  $\exp(-60000/T_e)$ .<sup>10</sup> This determination illustrates how the electronic state varies rapidly with temperature and thus will give the most sensitive measurements. The rotational fractions are extremely insensitive to temperature and therefore make these measurements very difficult. The temperature that was determined is plotted in Figure 12 versus the radial position of the plasma. The radial measurements were taken after correcting for the data and Abel inverting it to radial coordinates as in the previous sections. The fact that the rotational temperature dependence is weaker than the electronic and vibrational means that it will not significantly affect the shape or intensity of corresponding spectral features. Therefore, since the rotational temperature measurement falls within the accuracy of the experiment it follows that the plasma in the plenum is close to thermal equilibrium.



(a)



(b)

**Figure 4.10.-** Experimental and computed nitrogen rotational line spectra of the plenum air plasma. [a] 1.27 cm off-axis position and [b] 1.9 cm of-axis position.

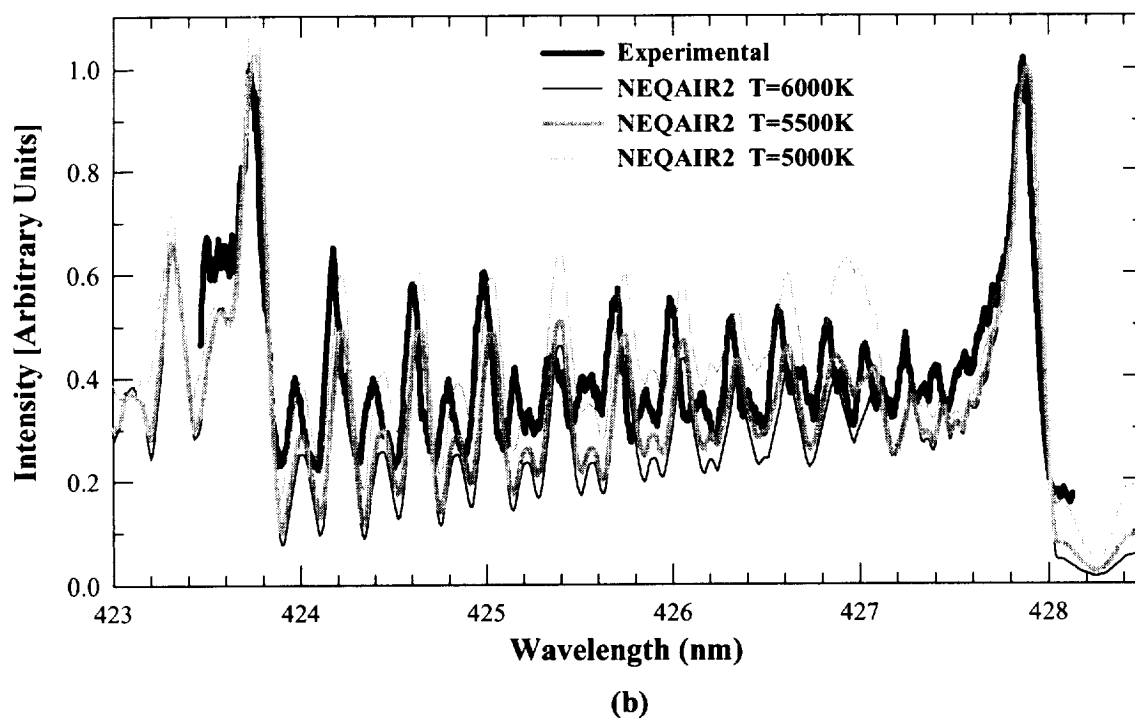
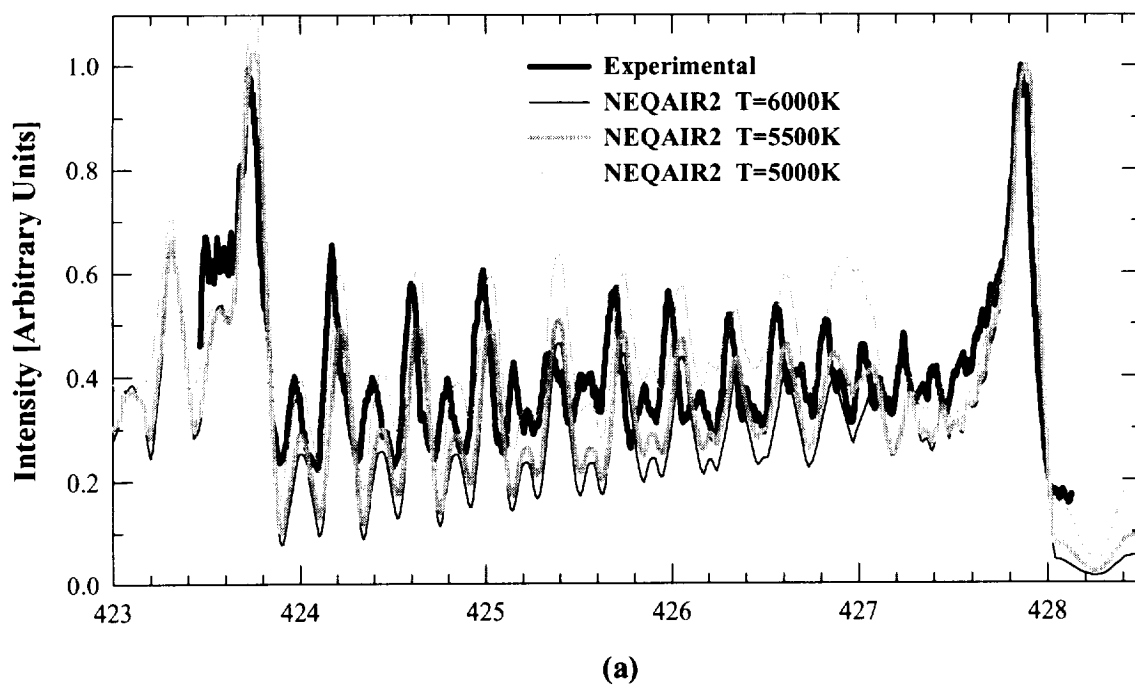


**Figure 4.11.-** Experimental and computed nitrogen rotational line spectra of the plenum air plasma. [a] 2.54 cm off-axis position and [b] 3.17 cm off-axis position.

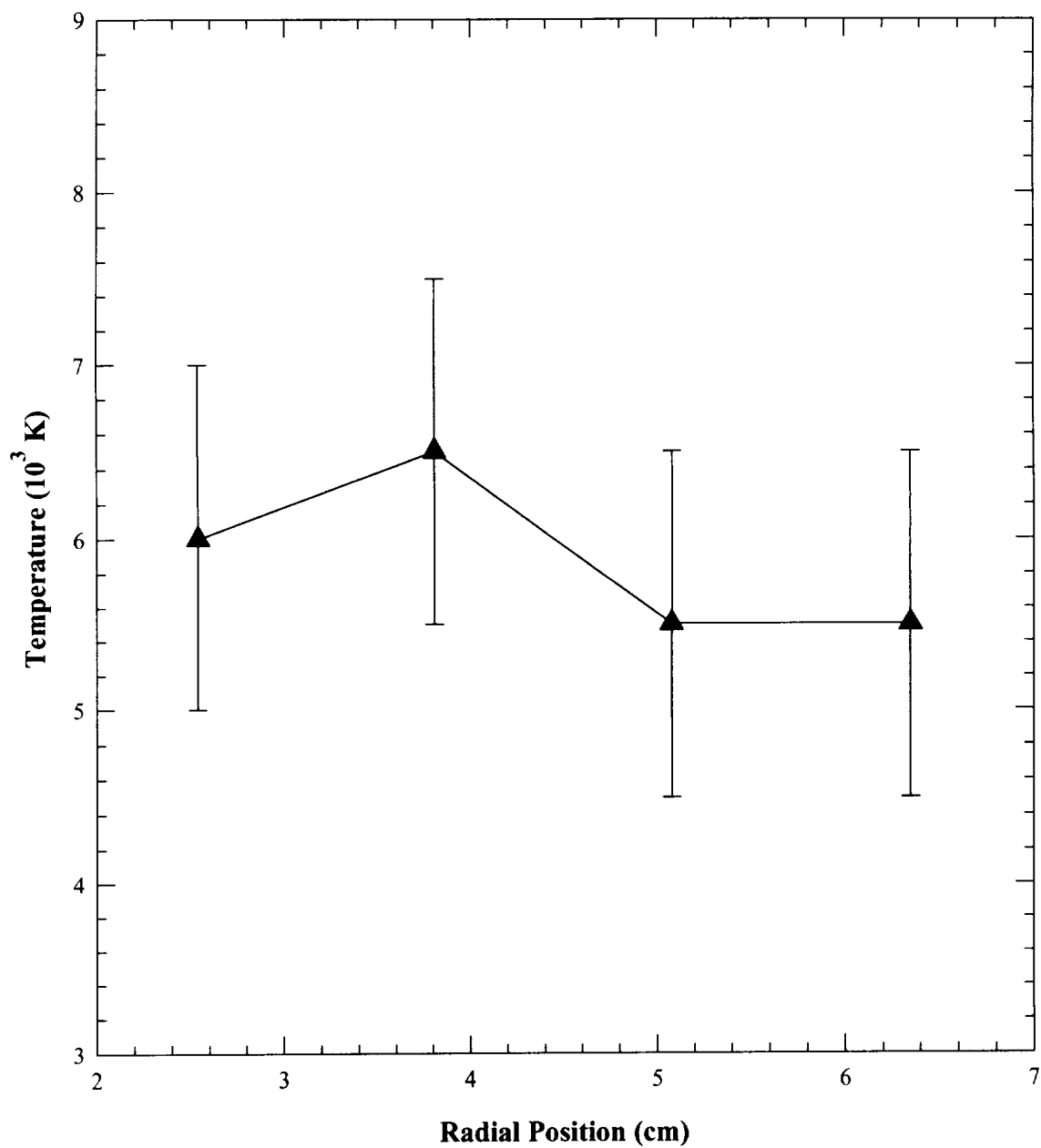


**Figure 4.12.-** Radial temperature profile of the nitrogen rotational spectra [ $\Delta v=1$ , (0,1)-(1,2) transitions].



## CHAPTER 5

### 5.1 Contributions of this thesis

Emission spectroscopy measurements were conducted in a 10 MW water cooled arc jet wind tunnel operating on a nitrogen and oxygen combination to simulate the earth's atmospheric conditions. The thermodynamic state of the plasma was studied by measuring electronic, vibrational and rotational temperatures from their excited transitional states. The vibrational and rotational states were analyzed using the NEQAIR2 code. The resulting composition showed that the plasma was approximately in local thermodynamic equilibrium, however, improvements to the data collection need to be made for further studies.

The experimental measurements were taken across the diameter of the plenum section of the arc jet heated wind tunnel by collecting emission radiation from a series of four positions. The object was to collect the spectrum from 2000 to 9000 Angstroms as a collimated "beam" across the plasma in order to perform Abel inversions and determine temperature profiles radially. The spectrum was corrected for spectral response and calibrated in intensity. It was then compared to the LTE calculations of the NEQAIR2 code<sup>10</sup>. The comparison was used as a guide to determine the deficiencies in the spectrum and illustrate some problems arising from calibration as well as collection techniques. It was determined that a calibration source constant in the ultraviolet spectrum is to be used with a source constant or intensity "flat" in the visible and infrared regions. Because such a combination was not available when these data were taken a lesser source was used for

calibration and NEQAIR, therefore, determined inconsistencies in the data.

Finally, temperature measurements were given in the range 4000 to 7500 K across the plasma in the plenum for the first time. These measurements will provide starting temperatures for plasma codes that predict the downstream temperatures and recombination rates. By improving the calibration this data can be more accurately used for these predictions.

## 5.2 Recommendations for future work

These measurements formed a foundation for plasma studies in the plenum region, however, much more analysis of the data should be performed. Also, the plasma should be characterized more by extending the number of collection points across the flow for Abel transformation purposes. As many as ten to twenty points should be measured for an accurate inversion equation. This would require modification of the plenum ring and probably would eliminate the fiber optic configuration with a single detector system and be replaced with a CCD array (visible) or focal plane array (infrared). The process could replace the complete spectrometer system with two-dimensional array systems by looking at isolated emission lines from the plasma field.

## REFERENCES

1. C. D. Scott, "Survey of Measurements of Flow Properties in Arcjets", Journal of Thermophysics and Heat Transfer, Vol.7, No.1, 1993.
2. M. A. Rob, L. H. Mack, S. Arepalli, C. D. Scott, "Spectral Measurements in the Plenum of an Arcjet Wind Tunnel", Final Report NASA/ASEE Summer Faculty Fellowship Program, NASA/JSC, 1994.
3. John D. Anderson, Jr., Hypersonic and High Temperature Gas Dynamics, McGraw-Hill Book Company, New York, NY (1989).
4. I. Terrazas-Salinas, C. Park, A. W. Strawa, N. K. M. Gopaul, and J. S. Taunk, "Spectral Measurements in the Arc Column of an Arc-Jet Wind Tunnel", 18<sup>th</sup> AIAA Aerospace Ground Testing Conference, AIAA 94-2595 (1994).
5. S. Arepalli, "Optical Diagnostics for the Arc Jet Facility at NASA/JSC", SPIE, Vol. 2005, June 1993.
6. W.C. Rochelle, H.H. Battley, J.E. Grimaud, D.J. Tillian, L.P. Murray, W.J. Lueke, and T.M. Heaton, "Orbiter TPS Development and Certification Testing at the NASA/JSC 10MW Atmospheric Reentry Materials and Structures Evaluation Facility," 21st AIAA Aerospace Sciences Meeting, AIAA-83-0147 (1983).
7. M.A. Rob & Larry H. Mack Jr., "Spectral Measurements in the Plenum of an Arcjet Wind Tunnel", 30th AIAA Thermophysics Conference, AIAA 95-2126(1995).
8. J. P. Lanquart, "The effect of light-pipes measurements on the determination of the emissivity by Abel Inversion," *J. Phys. D: Appl. Phys.* Vol.19, pp. 925-931, 1986.
9. H. R. Griem, Plasma Spectroscopy, McGraw-Hill Book Co., Inc. New York, NY (1964).
10. C. O. Laux, "Optical Diagnostics and Radiative Emission of Air Plasmas," Ph.D. Dissertation HTGL Report No. T-288, Department of Mechanical Engineering, Stanford University, Stanford, CA 94305, August, 1993.
11. Xiangli Chen, "Spectroscopic Diagnostics of Argon Plasmas During Laser-Gas Interaction," Master's of Science Thesis, Department of Mechanical Engineering, University of Illinois at Urbana-Champaign, 1988.

12. T. G. Owano, "Non-equilibrium behavior in a flowing, atmospheric pressure plasma," Ph.D. Dissertation, HTGL Report T-279, Department of Mechanical Engineering, Stanford University, Stanford, CA 94305, July 1991.
13. M. A. Akundi, "Temperature Determination of shock Layer Using Spectroscopic Techniques," Final Report NASA/ASEE Summer Faculty Fellowship Program, NASA/JSC, 1989
14. C.O. Laux, Private communications (1996).
15. L. H. Mack, M. A. Rob, S. A. Arepalli, C. D. Scott, C.O. Laux, "Radial Spectral Measurements in the Plenum of an Arcjet Wind Tunnel," 31st AIAA Thermophysics Conference, AIAA 96-1897(1996).